PPP2R2A insufficiency enhances PD-L1 immune checkpoint blockade efficacy in lung cancer through cGAS-STING activation

Zhaojun Qiu[# 1], No-Joon Song[# 2,3], Anqi Li [# 2,3], Deepika Singh[1], Chandra B. Prasad[1], Chunhong Yan[4], David P. Carbone [5], Qi-en Wang[1], Xiaoli Zhang[6], Zihai Li[2,3 *], Junran Zhang[1,3,7*]

Affiliations

1. The Department of Radiation Oncology, The Ohio State University Comprehensive Cancer Center and College of Medicine, Columbus, OH 43210, United States.
2. College of Medicine, The Ohio State University, Columbus, OH 43210, United States.
3. The James Comprehensive Cancer Center, Pelotonia Institute for Immuno-Oncology, The Ohio State University, Columbus, OH 43210, United States.
4. Georgia Cancer Center, Augusta University Medical College, 1410 Laney Walker Blvd., CN-2134, Augusta, GA 30912, United States.
5. James Comprehensive Cancer Center, The Ohio State University, 460 West 10th Avenue, Columbus, OH 43210, United States
6. USF Health, University of South Florida, Tampa, FL 33612, United States.
7.The James Comprehensive Cancer Center, Center for Metabolism, OH 43210, United States
#Contributed equally.

*Corresponding Authors

Address correspondence to: Junran Zhang, Department of Radiation Oncology at The Ohio State University, Biomedical Research Tower, Room 418, 460 W 12th Avenue, Columbus, OH 43210, USA. Phone: 614.293.2826.; Email: Junran.Zhang@osumc.edu. or Zihai Li, Pelotonia Institute for Immuno-Oncology, Pelotonia Research Center, Room 3123, 2255 Kenny Rd, Columbus, OH 43210, USA. Phone: 614.293.9966; Email: Zihai.Li@osumc.edu.

Conflict-of-interest statement

The authors have declared that no conflict of interest exists.

Abstract

PP2A B55α, a regulatory subunit of protein phosphatase 2 (PP2A), is underexpressed in over 40% of non-small cell lung cancer (NSCLC) cases due to loss of heterozygosity of *PPP2R2A*, the gene encoding this protein. Given that low PPP2R2A expression correlates with poor prognosis, treating PPP2R2A-deficient NSCLC represents an unmet medical need. Here, we show that *PPP2R2A* knockdown or its heterozygosity (*PPP2R2A*$^{+/-}$) increases cytosolic DNA, leading to cGAS-STING-type I interferon (IFN) pathway activation. PPP2R2A deficiency results in elevated expression of immune checkpoint protein PD-L1 via GSK-3β- and STING-dependent mechanisms. *PPP2R2A*$^{+/-}$ cancer cells have enhanced sensitivity to PD-L1 blockade in a mouse model of lung cancer due to modulation of the tumor immune microenvironment, resulting in increased NK cells and reduced infiltration and function of regulatory T cells (Tregs). Consequently, PD-L1 antibody treatment increases $CD8^+$ T infiltration and activity, especially in tumors with *PPP2R2A* heterozygosity. Further, systemic or Treg-specific IFNAR1 blockade reduces the efficacy of PD-L1 blockade in *PPP2R2A*$^{+/-}$ tumors. Patients with NSCLC with a low PPP2R2A/PD-L1 ratio respond better to immune checkpoint blockade (ICB). These findings underscore the therapeutic potential of ICB in treating PPP2R2A-deficient NSCLC while suggesting that PPP2R2A deficiency could serve as a biomarker for guiding ICB-based therapies.

Introduction

Lung cancer is the leading cause of cancer-related deaths in the U.S., with non-small cell lung cancer (NSCLC) representing ~80% of cases. Programmed cell death ligand 1 (PD-L1), an immune checkpoint protein, binds to programmed cell death protein 1 (PD-1) on T cells, causing dysfunction, while PD-1/PD-L1 antibodies block this interaction to restore antitumor activity. FDA-approved immune checkpoint blockade (ICB) therapies for NSCLC can be used alone or in combination (1). Yet, only a subset of patients respond, highlighting the need for biomarker-guided approaches to improve outcomes.

PP2A is a heterotrimeric serine/threonine phosphatase consisting of a catalytic subunit (C), a scaffold subunit (A), and one of 18 structurally distinct regulatory B subunits (2, 3). These subunits combine to form over 180 holoenzymes, each with unique substrate specificity and cellular localization (4), enabling PP2A to regulate diverse processes, including signal transduction, cell cycle progression, DNA replication, gene transcription, protein translation and DNA repair response (3-7). PP2A B55α, a regulatory B subunit of PP2A, is under expressed in over 40% of cases of NSCLC due to loss of heterozygosity (LOH) of *PPP2R2A* (8), the gene encoding this protein. Reduced B55α expression correlates with poor prognosis. Thus, targeting *PPP2R2A*-deficient lung cancer is an unmet medical need (8-11). Previous studies, including our own, have shown that *PPP2R2A* knockdown (KD) enhances the sensitivity of NSCLC and ovarian cancer to inhibitors targeting the cell cycle checkpoint protein CHK1 or ATR through its impact on the replication stress (RS) induced by oncogenic c-Myc (10, 12). In addition, PPP2R2A deficiency also increases the sensitivity of tumors to PARP inhibitors by phosphorylation-mediated regulation of ataxia-telangiectasia mutated (ATM) (8). Interestingly, PPP2R2A deficiency has been implicated in resistance to cisplatin (12, 13) and MEK inhibitors (14), highlighting its complex roles in cancer treatment. Despite these findings, the impact of *PPP2R2A* heterozygosity on ICB-based therapies remains unexplored.

The efficacy of ICB can be influenced by numerous factors. Cytosolic DNA sensing through the cyclic GMP-AMP synthase-stimulator of interferon genes (cGAS-STING) pathway plays a crucial role in PD-1 or PD-L1 blockade-based immunotherapy by promoting type I interferon (IFNs) expression (15, 16). Type I IFNs are a family of monomeric cytokines consisting of 14 IFNα subtypes, including IFNβ, IFNε, IFNκ, and IFNω. IFNα and IFNβ are the two major IFNs that have been extensively studied, whereas the functions of IFNε, IFNκ and IFNω remain poorly understood. Beyond bacterial and viral infections, this pathway can also be activated by cytosolic DNA from damaged mitochondria, certain parasites, cancer cells with genomic instability, and self-DNA released from damaged cells (17). Our previous study demonstrated that *PPP2R2A* KD increased RS and DNA double-strand breaks (DSBs) (10, 12). As RS is a major source of cytosolic DNA-mediated triggering of the cGAS-STING-IFN pathway and improves ICB efficacy in NSCLC (18, 19), it is plausible that *PPP2R2A* deficiency in tumor cells affects ICB outcomes by activation of the cGAS-STING-IFNs axis and the subsequent modulation of the tumor immune microenvironment (TME). However, this hypothesis remains untested.

Here, using both human NSCLC and mouse tumor cell line models, we demonstrate that *PPP2R2A* deficiency, achieved through either KD or heterozygous knockout (KO) (*PPP2R2A*$^{+/-}$) in NSCLC, results in cytosolic DNA accumulation and elevated PD-L1 expression via inhibitory

phosphorylation of GSK-3β and a STING-dependent mechanism. Consistent with our *in vitro* results, which show that *PPP2R2A* deficiency induces cytosolic DNA and activates the cGAS-STING-IFN pathway, *Ppp2r2a*$^{+/-}$ enhances the efficacy of PD-L1 antibody treatment *in vivo* in a syngeneic mouse model of NSCLC. By immune phenotyping we revealed that *Ppp2r2a*$^{+/-}$ tumor cells alter the immune cell composition within the TME, characterized by an increase in natural killer (NK) cells and a reduction in regulatory T cells (Tregs) infiltration compared to tumors with intact *Ppp2r2a*. We further found that following anti-PD-L1 antibody treatment, tumors derived from *Ppp2r2a*$^{+/-}$ cells exhibited increased infiltration of CD8^{+} T cells. In line with this observation, the enhanced antitumor effects of PD-L1 blockade in *Ppp2r2a*$^{+/-}$ tumors were dependent on CD4^{+} T cells, CD8^{+} T cells and NK cells. Furthermore, abrogation of type I IFN signaling through IFNAR1 blockade, either by systemic antibody treatment or specific genetic deletion in Treg cells, reversed the antitumor efficacy of PD-L1 blockade in *Ppp2r2a*$^{+/-}$ tumors. In summary, our findings reveal that *PPP2R2A*-deficient NSCLC cells, via activation of the cGAS-STING-IFN pathway, are more susceptible to anti-PD-L1-based therapy. Thus, PPP2R2A status in tumors may serve as a novel biomarker to guide patient selection for ICB-based therapies in the treatment of NSCLC.

Results

PPP2R2A deficiency leads to the accumulation of cytosolic DNA, activating the cGAS-STING pathway in mouse and human NSCLC cells

Results from our previous study suggest that *PPP2R2A* KD in the human NSCLC cell lines A549 and H1299 leads to increased RS and DSBs (10). To further determine the potential pathways that are affected by PPP2R2A deficiency, we conducted bulk RNA-sequencing (RNA-seq) analysis in the A549 cells with or without PPP2R2A KD (12) (**Supplementary Figure 1A**). GSEA analysis of this dataset suggested that interferon alpha response, inflammatory response, and interferon gamma response were enriched in *PPP2R2A* KD cells (**Supplementary Figure 1B**).

Given that the cGAS-STING-IFN pathway is activated by small DNA fragments in the cytoplasm induced by RS (20) and is important for the activation of inflammatory and IFNs signaling, we hypothesized that *PPP2R2A* deficiency activates cGAS-STING-IFN pathway via cytosolic DNA. To test our hypothesis, we generated *PPP2R2A* heterozygote (*PPP2R2A*$^{+/-}$) cell lines using both mouse and human lung cancer models because TCGA analysis shows that 53.3% of NSCLC cases have shallow PPP2R2A deletion, while ~4% exhibit deep deletion and PPP2R2A loss correlates with reduced expression (12). In addition, *PPP2R2A* shallow deletion is associated with an increased tumor mutational burden (TMB) (**Supplementary Figure 2A-C**), that is often associated with genomic instability because of damaged DNA and RS. Further, patients with NSCLC with shallow *PPP2R2A* deletions exhibit poorer prognoses (**Supplementary Figure 2D, E**), suggesting that the treatment of this subset of patients presents an unmet medical need.

It is worth noting that the analysis of TCGA-based data suggests that TMB is not associated with patient survival (*i.e.*, Disease-Specific Survival (DSS) and Disease-Free Interval (DFI)). After we controlled for the level of TMB in the Cox proportional hazard regression model, the association between PPP2R2A shallow deletion and patient survival in **Supplementary Figure 2** was slightly changed, but the difference did not reach a statistical significance (*P*-value for DFI = 0.15 and for DSS = 0.06 after controlling for TMB level) (**Supplementary Table 1**). Therefore, PPP2R2A deficiency, instead of TMB, might directly drive poor prognosis.

We next generated *PPP2R2A*$^{+/-}$ cells by targeting exon 3 of the gene using a CRISPR/Cas9 approach. PCR primers flanking exon 3 were used for characterizing the gene editing results in the transduced and selected cells. Deletion of exon 3 of both mouse *Ppp2r2a* and human *PPP2R2A* resulted in the expected frameshifts, leading to the degradation of full-length mRNA by nonsense-mediated mRNA decay (NMD) (**Supplementary Figure 3**). For mouse cells, genotyping results showed that single clones of *Ppp2r2a* heterozygous KO were successfully generated in the mouse lung tumor cell lines CMT167 and LLC (**Figure 1A**). However, no clones with homozygous depletion (*Ppp2r2a*$^{-/-}$) were generated, suggesting that Ppp2r2a is essential for mouse lung cancer cell survival, which is consistent with a previous report that complete loss of *Ppp2r2a* results in embryonic cell death (21). By immunoblotting we further confirmed the successful heterozygous KO of *Ppp2r2a* and revealed an increase in the levels of the DSB marker ϒH2AX in the two mouse lung cancer cells (**Figure 1B**). Using neutral comet assays, we further observed that the degree of DSBs were significantly elevated in CMT167 *Ppp2r2a*$^{+/-}$ cells. Representative results of comet assay are shown in **Figure 1C,** with

quantifications of Tail olive presented in **Figure 1D**. Furthermore, we measured the levels of cytosolic DNA using a SpectraMax Quant AccuClear Nano dsDNA Assay Kit and found greater accumulation of DNA in the cytoplasm in the heterozygous KO of *Ppp2r2a* compared to wild-type controls (**Figure 1E**). This finding was further verified by an upregulation of Histone H3 protein in the cytoplastic fraction (**Figure 1F, G**). We next stained for cytosolic DNA by Picogreen and DAPI in *Ppp2r2a*$^{+/-}$ CMT167 cells and found a greater percentage of cells with micronuclei (MN), which are an important source of cell-intrinsic immunostimulatory DNA via promotion of cGAS-STING-IFN (22), compared to *Ppp2r2a*$^{+/+}$ cells (**Figure 1H, I**).

We also generated human NSCLC cells with heterozygous (*PPP2R2A*$^{+/-}$) and homogeneous deletion (*PPP2R2A*$^{-/-}$) (**Supplementary Figure 4A, B**), which is different to what we observed in mouse cells where only *Ppp2r2a*$^{+/-}$ cells were able to be generated. In these *PPP2R2A* KO A549 cells, there was a markedly greater degree of DSBs compared to control cells (**Supplementary Figure 4C, D)**. Furthermore, we observed enhanced levels of cytosolic DNA and MN in both the heterozygous and homozygous deletion A549 cells compared to the control cells (**Supplementary Figure 4E, F, G**).

To validate the results observed in cells of the *PPP2R2A* KO clones, we conducted additional validations using pooled population cells with *PPP2R2A* KD in both mouse and human cells. In mouse cells, stable KD of *Ppp2r2a* in CMT167 and LLC cells led to increased RS compared to controls (**Supplementary Figure 5A**). In CMT167 cells with *Ppp2r2a* KD, we observed a significant increase in DSBs (**Supplementary Figure 5B, C**) and cytosolic DNA accumulation compared to controls (**Supplementary Figure 5D**). Additionally, histone H3 was notably upregulated in the cytoplasmic fraction (**Supplementary Figure 5E, F**), and we observed an increased percentage of cells with MN (**Supplementary Figure 5G, H**). Similarly, *PPP2R2A* KD in our two human lung cancer cell lines resulted in elevation of RS (**Supplementary Figure 6A**), as we previously reported(23)**.** In A549 cells with low PPP2R2A expression (10), we noted an increase in DSBs (**Supplementary Figure 6B, C**), higher cytosolic DNA levels (**Supplementary Figure 6D**), and a greater percentage of cells with MN (**Supplementary Figure 6E, F**). Additionally, we further examined cytosolic DNA levels in four NSCLC cell lines: A549, H838, SK-MES-1, and H1437. Among them, SK-MES-1 and H1437 exhibited higher levels of cytosolic DNA (**Supplementary Figure 7A, B**), which correlates with their lower PPP2R2A expression resulting from loss of heterozygosity (8). Therefore, PPP2R2A deficiency causes cytosolic DNA accumulation, activating the cGAS-STING pathway in mouse and human NSCLC cells

PPP2R2A **/*Pppp2r2a* downregulation activates the cGAS-STING pathway to trigger type I IFN production in lung cancer cells**

To investigate whether the accumulation of cytosolic DNA in cells with PPP2R2A deficiency activates the cGAS-STING-IFN pathway, we first measured the phosphorylation status of the key components of the cGAS-STING pathway. We found higher p-STING, p-STAT, p-TBK and p-IRF3 levels in *Ppp2r2a*$^{+/-}$ CMT167 and LLC cells compared to *Ppp2r2a*$^{+/+}$ cells (**Figure 2A, B**). In line with these results, we found significant upregulation of IFNα, β, and other several downstream factors of IFNs assessed by qPCR in CMT167 (**Figure 2C**). In contrast, PPP2R2A deficiency in LLC cells resulted in no obvious increase in type I IFN. Similarly, we observed increased of expression levels of key markers of cGAS-STING pathway activation in

PPP2R2A$^{+/-}$ and *PPP2R2A*$^{-/-}$ A549 and H1299 cells (**Figure 2D, E**). Also, we found that there was an elevation of type I IFN expression in A549 *PPP2R2A*$^{+/-}$ and *PPP2R2A*$^{-/-}$ but not in H1299 *PPP2R2A*$^{+/-}$ and *PPP2R2A*$^{-/-}$ cells compared to their respective controls (**Figure 2F**).

To further confirm these observations in cell clones with *Pppp2r2a* KO, we next investigated the effects of stable *Ppp2r2a* KD on cGAS-STING-IFN pathway activation in CMT167 and LLC cells. We found that lower expression of Ppp2r2a achieved by two different shRNAs resulted in higher levels of cGAS-STING pathway proteins in both CMT167 and LLC cells along with elevated cGAS and STING expression, as compared to control cells (**Supplementary Figure 8A, B**). These results are in alignment with previous reports showing that both STING and cGAS are downstream factors of cGAS-STING (24, 25). Notably, although we observed increased expression of type I IFN in CMT167 *Ppp2r2a* KD cells, nearly none of the tested IFNs and downstream factors, except for *Mx1*, were higher in LLC *Ppp2r2a* KD cells compared to control cells (**Supplementary Figure 8C**). Thus, the activation of the cGAS-STING pathway may not necessarily lead to the production of IFN signaling. Simply detecting the phosphorylation status of downstream cGAS-STING factors without assessing IFN generation may lead to an underestimation of the complete activation of the cGAS-STING-IFN pathway. Like mouse CMT167 cells, *PPP2R2A* KD in the human cell line A549 resulted in activation of the cGAS-STING (**Supplementary Figure 8D, E**) and type I IFN pathways and the latter's downstream factor expression (**Supplementary Figure 8F**). Furthermore, by ELISA, we found that both *PPP2R2A/Pppp2r2a* KD and KO significantly increased the secretion of IFN-β and/or IFN-α in human A549 cells (**Supplementary Figure 9A, B**) and mouse CMT167 cells (**Supplementary Figure 9C–F**), as measured in *in vitro* culture supernatants. Consistent with these results, we found elevated levels of IFN-β and/or IFN-α in the serum of *Ppp2r2a*$^{+/-}$ tumor-bearing mice (**Supplementary Figure 9G, H**).

Taken together, our results suggest that PPP2R2A deficiency induces RS and cytosolic DNA accumulation, which subsequently activates the cGAS-STING-IFNs pathway, suggesting a potential mechanistic link between genetic loss of *PPP2R2A*, cytosolic DNA accumulation and immune signaling pathway activation. However, it is context-dependent, as no significant increase in type I IFN was detected in PPP2R2A-deficient LLC and H1299 cells.

PPP2R2A deficiency results in increased PD-L1 expression via GSK-3β- and cGAS-STING-dependent mechanisms

PD-L1 (B7-H1) is a 33 kDa transmembrane protein, but in tumor cells it is typically detected at ~45 kDa due to glycosylation, which stabilizes PD-L1 by preventing GSK3β-mediated phosphorylation and degradation (26). To assess PD-L1 glycosylation, we treated cells with PNGase F, which reduced the ~45 kDa band to 33 kDa, confirming that the predominant form of PD-L1 in our cancer cell lines is glycosylated (**Supplementary Figure 10A-D).**

Findings in our previous report suggested that *PPP2R2A* KO leads to an increase in the inhibitory phosphorylation of GSK-3β (p-GSK-3β-ser9) (12), and here we also found that PPP2R2A deficiency leads to cGAS-STING pathway activation (**Figure 2**). Thus, we next determined the status of PD-L1 expression in *PPP2R2A*$^{+/-}$ cells and also investigated whether both mechanisms (elevations of p-GSK-3β-ser9 and activation of cGAS-STING) are involved in regulation of PPP2R2A deficiency-induced PD-L1 expression. In heterozygous CMT167 and

LLC cells, we found higher PD-L1 protein expression, along with higher levels of p-GSK-3β-ser9, especially in CMT167 heterozygous cells, compared to wild-type controls **(Figure 3A, B**). Additionally, in pooled *Ppp2r2a* KD populations, we found higher PD-L1 and p-GSK-3β-ser9 levels in both CMT167 and LLC mutant cells compared to controls (**Supplementary Figure 11A, B**).

Supporting the above mouse data, we found similar results in human cells. In particular, the protein levels of PD-L1 were higher in *PPP2R2A*$^{+/-}$ and *PPP2R2A*$^{-/-}$ A549 and H1299 cells compared to their respective controls (**Figure 3C, D**). The levels of p-GSK-3β-ser9 were also higher in the heterozygous and homozygous *PPP2R2A* KO cells compared to the control cells (**Figure 3C, D**). We found that PPP2R2A deficiency leads to an upregulation of PD-L1. PD-L1 protein expression, as well as p-GSK-3β-ser9 were elevated at the protein level in *PPP2R2A* KD A549 and H1299 cells (**Supplementary Figure 11D, E**). PD-L1 mRNA levels were also increased in *PPP2R2A* KD A549 cells (**Supplementary Figure 11F**). Together, these results suggest that PPP2R2A deficiency leads to increased PD-L1 expression, which is associated with increased p-GSK-3β-ser9 expression. Thus, GSK-3β, especially p-GSK-3β-ser9, may be involved in the PPP2R2A deficiency-induced elevation of PD-L1 expression.

To directly test this hypothesis, we next determined if phosphorylation of GSK-3β is required for PPP2R2A deficiency-induced PD-L1 expression. Stable KD of the gene encoding GSK-3β reduced the Ppp2r2a deficiency-induced upregulation of PD-L1 in CMT167 cells (**Figure 3E**), with the same effect observed in A549 cells with GSK-3β KD (**Figure 3F**). In addition, in A549 cells, stable overexpression of the GSK-3β-S9A phosphorylation-defective mutant increased PD-L1 protein levels, while *PPP2R2A* KD had no further effect on PD-L1 expression in these cells (**Figure 3G**). Moreover, the expression of exogenous PPP2R2A in H1437 cells, which have PPP2R2A deficiency due to loss of heterozygosity, led to lower levels of p-GSK-3β-ser9 (**Supplementary Figure 11G, H**). Furthermore, transient KD of GSK3β in both A549 *PPP2R2A*$^{+/-}$ and *PPP2R2A*$^{-/-}$ (**Supplementary Figure 12A, B**) and CMT167 *Ppp2r2a*$^{+/-}$ cell lines (**Supplementary Figure 12C, D**) resulted in a reduction of PPP2R2A deficiency-induced PD-L1 expression, compared to cells with intact GSK-3β. Together, these results support the notion that GSK-3β (p-GSK-3β-ser9) is required for PPP2R2A deficiency-induced PD-L1 upregulation.

Additionally, PPP2R2A deficiency-induced PD-L1 can also be regulated at the transcriptional level by the activation of cGAS-STING-type I IFN pathway (27-29). Activation of the cGAS–STING pathway has been shown to upregulate PD-L1 expression (29). Given the increased cGAS-STING pathway activation in cells with PPP2R2A deficiency (**Figure 2**), we first determined how PPP2R2A deficiency affects PD-L1 expression at the mRNA level. We found that *Ppp2r2a* heterozygosity leads to the increased expression of PD-L1 mRNA level in CMT 167 cells; however, the increased expression of PD-L1 mRNA level was not observed in LLC cells (**Figure 3H and Supplementary Figure 11C**), suggesting the upregulation of PD-L1 in cells with PPP2R2A deficiency could be due to protein and/or transcriptional regulation. Similarly, PD-L1 expression was elevated at the mRNA level in *PPP2R2A* KO and KD A549 and H1299 cells, though a much less significant was observed in H1299 cells compared to A549 cells (**Figure 3I and Supplementary Figure 11F**). In LLC cells, transcriptional regulation may not be involved.

To directly test if the cGAS-STING pathway is involved in PD-L1 expression, we next investigated whether *STING* KO diminishes PD-L1 expression in cells with low PPP2R2A or Ppp2r2a expression. We generated a cell clone with *STING* KO using CRISPR/cas9. We found that PD-L1 protein upregulation triggered by *Ppp2r2a* KD was decreased in *Sting* KO CMT167 cells (**Figure 3J and Supplementary Figure 13A**). The KD of *Ppp2r2a* failed to upregulate PD-L1 mRNA in *Sting*-KO CMT167 cells (**Figure 3K and Supplementary Figure 13B)**. Similar results were also observed in *STING* KO A549 cells (**Figure 3L, M and Supplementary Figure 13C-E**). Therefore, it is likely that the cGAS-STING pathway-mediated PD-L1 expression also contributes to the increased PDL-1 expression observed in PPP2R2A deficient cells. Flow cytometric analysis further revealed that cell surface PD-L1 expression was elevated in *Ppp2r2a*$^{+/-}$ CMT167 cells *in vitro* (**Supplementary Figure 14A-C**). Together, these data suggest that PPP2R2A deficiency leads to increased PD-L1 expression at the protein and/or mRNA levels. The inactivation of GSK-3β, along with the activation of the cGAS-STING-type I IFN pathway, could contribute to the increase in PD-L1 expression induced by PPP2R2A deficiency.

In summary, PPP2R2A deficiency induces PD-L1 expression through two mechanisms: inhibitory phosphorylation of GSK3β (Ser9), which increases PD-L1 at the protein level across all tested cells, and activation of the cGAS–STING pathway, which upregulates PD-L1 at the mRNA level in a cell context–dependent manner. For example, both mechanisms operate in CMT167 and A549 cells, whereas only GSK3β (Ser9) acts in LLC cells. Despite these differences, PPP2R2A deficiency consistently increases PD-L1 expression.

Ppp2r2a deficiency enhances PD-L1 blockade efficacy

We next examined the effect of Ppp2r2a heterozygosity on tumor growth and responses to an antibody against PD-L1 in syngeneic host C57BL/6J mice, where CMT167 and LLC cells were originally derived from. We first treated mice bearing *Ppp2r2a*$^{+/+}$ and *Ppp2r2a*$^{+/-}$ CMT167 tumors with control antibodies or anti-PD-L1 antibodies (100 μg, three doses) (**Figure 4A**). In mice with control tumors (*Ppp2r2a*$^{+/+}$), we found no significant anti-tumor response following PD-L1 blockade. In addition, *Ppp2r2a* heterozygous KO alone did not affect tumor growth in the presence of control antibodies (**Figure 4B**). However, within one-week, we did observe substantial tumor regression in the mice bearing *Ppp2r2a*$^{+/-}$ tumors that were treated with PD-L1 blockade. They remained the lowest among the four groups (**Figure 4B, C**). The growth curves of each group are demonstrated in **Figure 4D-G**. Additionally, PD-L1 blockade significantly improved the survival of mice bearing *Ppp2r2a* heterozygous KO CMT167 cells (**Figure 4H)**. The dosage of control and anti-PD-L1 antibodies did not affect the body weight of C57BL/6 mice. Body weights for each group, recorded on day 0 and at the cutoff date, are shown in **Figures 4I** and **4J**. Thus, we conclude that *Ppp2r2* heterozygous depletion potentiates the efficacy of PD-L1 blockade *in vivo* in our CMT167 cell line model of NSCLC.

It is worth noting that, consistent with our observation that PPP2R2A deficiency leads to increased PD-L1 expression *in vitro* (**Figure 3, Supplementary Figure 11, 14A-C**), flow cytometric analysis further revealed that cell surface PD-L1 expression was elevated in *Ppp2r2a*$^{+/-}$ CMT167 tumors *in vivo* (**Supplementary Figure 14D-E**).

We next determined the impact of *Ppp2r2a* heterozygosity on PD-L1 antibody treatment in LLC cells, a cell line showing no obvious upregulation of IFNs (**Supplementary Figure 15A**). *Ppp2r2a* heterozygous KO significantly suppressed LLC tumor growth (**Supplementary Figure 15B, C**); however, PD-L1 blockade failed to sensitize *Ppp2r2a*$^{+/-}$ cells to the effects of the PD-L1 antibody, which is similar to what was seen in *Ppp2r2a*$^{+/+}$ cells (**Supplementary Figure 15B, D-G**). Expectedly, given these results, PD-L1 blockade did not prolong the survival of the mice bearing LLC tumors (**Supplementary Figure 15H**). Body weight data for each group are presented in **Supplementary Figure 15I and 15J.** This result aligns well with the failure to activate IFN signaling despite increased RS in LLC cells (**Figure 2C**, **Supplementary Figure 8C**), further supporting our hypothesis that cGAS-STING-IFN signaling plays a crucial role in the response to ICB.

Thus, our results suggest that cGAS-STING-IFN activation, instead of merely cGAS-STING activation, is important to the antitumor immune response. In LLC cells, although activation of the cGAS–STING pathway is evidenced by increased phosphorylation of key signaling components (**Figure 2A, B** and **Supplementary Figure 8A, B**), the expression of the tested type I IFN-related genes shows no increase for reasons that are not yet clear (**Figure 2C and Supplementary Figure 8C**). Consequently, PPP2R2A deficiency-induced PD-L1 mRNA levels in these cells do not increase to the same extent as observed in CMT167 cells. Therefore, in CMT167 cells, PPP2R2A deficiency induces cGAS–STING–IFN activation and increases sensitivity to PD-L1 antibody, whereas in LLC cells, cGAS–STING activation occurs without a substantial increase in type I IFN and dramatic impact on PD-L1 antibody sensitivity.

Lastly, in support of the result showing that PPP2R2A deficiency/low expression increases PD-L1 expression and enhances the efficacy of anti-PD-L1 ICB (**Figure 3 and 4**), we found that patients with a low PPP2R2A/PD-L1 ratio in their cancer had improved overall survival when treated with immune checkpoint inhibitors, including antibodies targeting PD-L1 (**Supplementary Figure 16A**), PD1 (**Supplementary Figure 16B**), and CTLA4 (**Supplementary Figure 16C**). Similarly, by progression-free survival analysis, we found that patients with a low PPP2R2A/PD-L1 ratio demonstrated enhanced therapeutic efficacy to PD-L1 antibodies (**Supplementary Figure 16D**), PD-1 antibodies (**Supplementary Figure 14E**), and CTLA4 antibodies (**Supplementary Figure 16F**). Together, these results indicate that PPP2R2A deficiency or low expression, particularly accompanied by increased PD-L1 expression, enhances the response to ICB.

Deficiency in Ppp2r2a in tumor cells enhances the efficacy of PD-L1 blockade by modifying the TME via increasing NK cell infiltration, and reducing Treg cell infiltration

We, thus, next determined the cellular mechanisms underlying the enhanced antitumor efficacy for the PD-L1 blockade in *Ppp2r2a*$^{+/-}$ CMT167 tumors via multispectral flow cytometry according to the regimen described in **Figure 5A**. One day after administering the third antibody dose, tumors were harvested and tumor infiltrating lymphocytes (TILs) were isolated using Percoll gradient separation, followed by extensive phenotypic analyses using multispectral flow cytometry (CyTek) with a comprehensive immune panel comprising 26 markers to define myeloid and lymphoid lineages. These antibodies include markers to identify T cell, B cell, DCs and macrophages. The panel included antibodies against CD45, CD3, CD4, CD8, B220,

CD11b, CD11c, NK1.1, Ly6C, F4/80, MHC class II, PD-1, CD24, CD103, Foxp3, CD64, CD206, Arg1, CD25, PD-L1, TCRb, CD38, CD172, XCR1, Ly6G and CD19. The gating strategy used in this research is shown in **Supplementary Figure 17**.

To visualize tumor-infiltrating immune cell populations, we gated live $CD45^+$ immune cells and performed opt_SNE dimension reduction and FlowSOM clustering, and we annotated key populations (**Figure 5B)**. To compare population dynamics across the experimental groups we generated contour plots and observed increased accumulation of NK cells along with decreased Treg accumulation in *Ppp2r2a*$^{+/-}$ tumor samples (**Figure 5C**). To validate our observations, we generated 2D flow cytometry plots to identify NK cells ($CD3^-$ $NK1.1^+$), Tregs ($FoxP3^+$ $CD25^+$) and $CD8^+$ T cells ($CD8^+$ $CD4^-$). Statistical analysis and representative figures indicate that *Ppp2r2a*$^{+/-}$ tumors were associated with greater NK cell infiltration (**Figure 5D**) and lower Treg cell infiltration (**Figure 5E**) even before PD-L1 antibody treatment. These results suggest that *Ppp2r2a* heterozygosity in tumors reshapes the TME. PD-L1 antibody treatment caused a significant increase in the proportion of cytotoxic $CD8^+$ cells among *Ppp2r2a*$^{+/-}$ cells (**Figure 5F**), compared to tumors with intact *Ppp2r2a*. Given that *PPp2r2a* heterozygosity also leads to increased PD-L1 expression, which has a potential to suppress T cell activity, it is most likely that *Ppp2r2a* heterozygosity causes a double-edged impact on the TME. Namely, on the one hand it has a positive impact on antitumor activity by increasing NK cell infiltration and decreasing Treg infiltration, but on the other hand, it has a negative impact on antitumor activity by triggering increased PD-L1 expression. But overall, the impact appears to be positive as such heterozygosity appears to potentiate anti-PD-L1-based therapy (**Figure 5G**).

Next, we evaluated the phenotype of $CD8^+$ T cells using the same experimental schedule (**Supplementary Figure 18A**). We gated live $CD45^+CD3^+CD8^+$ cells from four groups and applied UMAP dimension reduction and FlowSOM clustering to identify clusters with distinct marker expression patterns (**Supplementary Figure 18B)**. Naïve-like $CD8^+$ T cells ($CD44^-$ $CD62L^+$) is a type of T cell that has not yet been fully activated, and the proportion of this subset was lower in the *Ppp2r2a*$^{+/-}$ group compared to the *Ppp2r2a*$^{+/+}$ group, with a trend that PD-L1 blockade further decreased their proportion by activating this subset (**Supplementary Figure 18B).**

Further analysis of multiple suppressive markers revealed that the suppressive phenotype of Tregs was diminished in the *Ppp2r2a*$^{+/-}$ group, compared to *Ppp2r2a*$^{+/+}$ (**Supplementary Figure 18C-G)**. This result suggests that the Treg cells have an impaired function. To further address this point, we co-cultured Tregs cells derived from *Ppp2r2a*$^{+/-}$ or *Ppp2r2a*$^{+/+}$ tumors, with wild type $CD8^+$ T cells to assess Treg suppressive capacity. $CD8^+$ T cell proliferation, measured by CellTrace Violet–based flow cytometry, was significantly higher in the *Ppp2r2a*$^{+/-}$ group compared with the *Ppp2r2a*$^{+/+}$ group (**Supplementary Figure 18H, I**). Therefore, Treg activity is suppressed in *Ppp2r2a*$^{+/-}$ tumors. Altogether, *Ppp2r2a* heterozygosity enhances the efficacy of PD-L1 blockade tumors by reshaping the TME, particularly through stronger suppression of Tregs induced by *Ppp2r2a* deficiency.

$CD8^+$ T cells, $CD4^+$ T cells and NK cells are required for the Ppp2r2a deficiency-induced increase in PD-L1 antibody efficacy

Based on our findings that *Ppp2r2a* heterozygosity in tumors leads to an increased infiltration of NK cells while reducing Treg cell infiltration and that *Ppp2r2a* heterozygosity combined with PD-L1 blockade results in tumor regression in mice and an increase in the proportion of $CD8^+$ T cells, we hypothesized that $CD8^+$ T cells, $CD4^+$ T cells, and NK cells are necessary for the antitumor efficacy induced by Ppp2r2a deficiency and PD-L1 blockade. To test this hypothesis, *Ppp2r2a*$^{+/-}$ tumor-bearing mice were treated with control or PD-L1 antibodies while NK cells, $CD4^+$, $CD8^+$, and $CD4/8^+$ T cells were depleted using depletion antibodies (**Figure 6A**). Among all the treatment groups, the PD-L1 antibody alone group exhibited the slowest tumor growth. However, depletion of these immune cell types abolished the inhibitory effect on tumor growth observed in the PD-L1 blockade monotherapy group (**Figure 6B**). Tumor growth curves for each group are demonstrated in **Figure 6C-H**. The reductions in tumor volume (**Figure 6I**) and weight (**Figure 6J**) observed in the PD-L1 blockade group were reversed when $CD8^+$ T cells, $CD4^+$ T cells and $CD4/8^+$ were depleted. These results demonstrate that $CD8^+$ T cells, $CD4^+$ T cells, and NK cells are required for the efficacy of PD-L1 blockade in mice bearing *Ppp2r2a*$^{+/-}$ tumors. Of note, both helper T cells ($CD4^+$ T cells) and regulatory T cells (Tregs) express CD4 on their surface. Thus, CD4 depletion by this antibody approach depletes both types of immune cells.

Blocking IFN signaling by IFNAR1 neutralization abolishes the anti-tumor efficacy of a PD-L1 antibody in *Ppp2r2a*$^{+/-}$ KO CMT167 tumors

To determine whether type I IFN signaling contributes to Ppp2r2a deficiency-induced sensitivity to PD-L1 antibody treatment, we blocked type I IFN signaling using an anti-IFNAR1 antibody and assessed its impact on PD-L1 antibody efficacy in treating *Ppp2r2a*$^{+/-}$ tumors (**Figure 7A**). The abrogation of type I IFN signaling by the IFNAR antibody reversed the antitumor efficacy of PD-L1 blockade in *Ppp2r2a*$^{+/-}$ CMT167 tumors (**Figure 7B**). The growth curves for individual tumors of each group are presented in **Figure 7C-J**. Moreover, the reductions in tumor volume (**Figure 7K**) and weight (**Figure 7L**) observed in the PD-L1 blockade group on the cutoff day were also abolished when IFNAR1 was simultaneously blockaded. Thus, in support of the role of type I IFNs in the Ppp2r2a heterozygosity-induced potentiation of PD-L1 efficacy, IFNAR1 neutralization abrogates *Ppp2r2a* heterozygosity-related PD-L1 antibody sensitivity.

To further evaluate the role of type I IFN signaling in Tregs, we adoptively transferred either wild-type or *Ifnar*-deficient Tregs into diphtheria toxin–pretreated Foxp3-DTR mice. Briefly, we modified this Treg replacement protocol in which Foxp3-DTR mice were treated daily with diphtheria toxin (DT) to deplete endogenous Tregs and then reconstituted the mice with Tregs from either wild-type or *Ifnar1*$^{-/-}$ donors. We then implanted *Ppp2r2a*$^{+/-}$ cells into the host followed by treatment with the PD-L1 antibody (**Supplementary Figure 19A**). Compared to the group with wild-type Treg reconstitution, the group with *Ifnar1*$^{-/-}$ Treg reconstitution exhibited blunted PD-L1 antibody's anti-tumor activity, suggesting that without the IFNAR signal in Treg cells, Treg cells had more of an inhibitory effect which promoted the tumor growth (**Supplementary Figure 19B, left panel**) and as a feedback loop, there were more Tregs infiltrating into the TME (**Supplementary Figure 19B,** right panel). This suggests that type I IFN signaling in Tregs contributes to the efficacy of anti-PD-L1 in eliminating Ppp2r2a-deficient tumor cells.

To further illustrate the phenotype of tumor infiltrating Tregs, we performed a high-dimensional flow cytometry analysis on the tumor infiltrating Tregs and displayed the data in two dimensions by performing dimension reduction using the Uniform Manifold Approximation and Projection (UMAP) approach (**Supplementary Figure 19C**). Unsupervised clustering analysis with FlowSOM enabled differential expression analysis between groups, identifying 17 distinct clusters. The percentage of clusters 12 and 13 was significantly enriched in mice reconstituted with *Ifnar1*$^{-/-}$ Tregs and bearing *Ppp2r2a*$^{+/-}$ tumors (**Supplementary Figure 19C**, left). These two clusters shared the characterization of increased CD39, ICOS, CLTA-4, CD44 and GITR, indicating that this subset of Tregs exhibited more suppressive phenotype (**Supplementary Figure 19D**).

The CD8$^+$ T cell phenotype of PD-L1 antibody-treated mice bearing *Ppp2r2a*$^{+/-}$ tumors in the presence and absence of blocking IFNs signaling by IFNAR1 neutralization

Lastly, we investigated the role of type I IFN signaling in the therapeutic efficacy of PD-L1 blockade in mice bearing *Ppp2r2a*$^{+/-}$ tumors, particularly in relation to that of CD8$^+$ T cells, as we detected differences in Treg phenotype. To address this, mice were implanted with either *Ppp2r2a*$^{+/-}$ or *Ppp2r2a*$^{+/+}$ tumors and treated with the anti-PD-L1 antibody, an anti-IFNAR1 antibody, or a combination of both antibodies (aPD-L1 + aIFNAR1) (**Figure 8A**). We gated live CD8$^+$ T cells, followed by UMAP dimension reduction and FlowSOM clustering, to define distinct subpopulations (**Figure 8B**). The heatmap of the clusters displayed in **Figure 8B** is shown in **Supplementary Figure 20**. Key marker expression patterns were overlaid onto the UMAP space to characterize each cluster (**Figure 8C**). Contour plots were generated to visualize population dynamics, revealing a notable increase in CD44$^+$Cx3cr1$^+$CD8$^+$ T cells exclusively in the aPD-L1-treated *Ppp2r2a*$^{+/-}$ tumor-bearing mice, highlighted by the blue dotted line (**Figure 8D**). This subset exhibited intermediate PD-1 expression along with no or low expression of other inhibitory markers, suggesting that they are effector/activated cells (30-33). The increase of cytotoxic CD8$^+$ T cells (CD44$^+$Cx3cr1$^+$CD8$^+$ T) after aPD-L1 antibody treatment suggests that a highly developed and strongly activated subset of cytotoxic T cells was increased only in PD-L1antibody treated *Ppp2r2a*$^{+/-}$ tumors**.** In support of this observation, Indeed, we measured IFN-γ and TNF-α expression in re-stimulated single-cell suspensions from *Ppp2r2a*$^{+/+}$ and *Ppp2r2a*$^{+/-}$ tumor samples by intracellular staining (**Supplementary Figure 21A**). CD8$^+$ T cells from *Ppp2r2a*$^{+/-}$ tumors produced higher levels of both cytokines. Additionally, IL-2$^-$ Perforin$^+$ T cells were also dramatically increased in the PD-L1 antibody treated *Ppp2r2a*$^{+/-}$ tumors (**Supplementary Figure 21B-D**). These results indicate enhanced polyfunctionality of CD8$^+$ T cells, especially in the PD-L1 antibody-treated group. Notably, this expansion of cytotoxic CD8$^+$ T cells in aPD-L1-treated mice with *Ppp2r2a*$^{+/-}$ tumors was abolished upon IFNAR1 blockade, underscoring the critical role of type I IFN signaling in the formation of this subset (**Figure 8E, F**).

In summary, our findings support a model where PPP2R2A deficiency in NSCLC enhances the efficacy of PD-L1 ICB through activation of the cGAS-STING-IFNs pathway. Tumor PPP2R2A deficiency reprograms the TME by increasing NK cell infiltration, reducing Treg cell infiltration, and upregulating PD-L1 expression. These changes in the TME make PPP2R2A-deficient tumors more responsive to PD-L1 blockade therapy (**Figure 8G**).

Discussion

Tumor cells frequently harbor unique genetic alterations that influence therapeutic responses. In this study, we report that heterogeneous alterations in *PPP2R2A* reshape the TME by increasing the proportion of NK cells, reducing Tregs and elevating PD-L1 expression. These changes occur via the activation of the cGAS-STING-IFN pathway. *PPP2R2A*-deficient tumors were more responsive to PD-L1 blockade, indicating that *PPP2R2A*-deficient NSCLC may be effectively targeted with PD-L1-associated ICB. Thus, *PPP2R2A* deficiency holds the potential to be a predictive biomarker for the efficacy of ICB in treating NSCLC.

Double-stranded DNA in the cytoplasm of eukaryotic cells serves as a primary trigger for cGAS-STING activation. PPP2R2A is implicated in homologous recombination (HR) repair (8). Moreover, PPP2R2A deficiency leads to oncogene-induced RS and DNA damage (10, 11). Consistent with the concept that RS and DNA damage produce cytosolic DNA—a critical driver of cGAS-STING activation—PPP2R2A deficiency increases cytosolic DNA and MN formation, which are associated with activation of the cGAS-STING-IFN pathway.

We acknowledge that one limitation of our study is that the precise mechanisms by which RS activates cGAS in PPP2R2A deficient cells remain unclear. However, previous studies have suggested that RS can promote cGAS activation through cytosolic DNA (20, 34, 35). When replication forks stall under stress, they become fragile and susceptible to degradation. This process can release single- and double-stranded DNA fragments into the cytoplasm, activating cGAS. In addition, cytosolic DNA can appear as MN, which forms following cell division due to RS (36). When the MN envelope ruptures, cGAS can recognize the escaped DNA and trigger an immune response (22, 37, 38). Thus, MN may represent a source of cytosolic DNA that activates the cGAS–STING pathway in PPP2R2A-deficient cells. However, whether MN is directly linked to cGAS activation remains debated (39, 40). As MN are only one form of cytosolic DNA, RS can also cause nuclear DNA release in other forms that activate cGAS–STING–IFN signaling (41). Therefore, RS-induced cytosolic DNA, whether as MN or other forms, has the potential to trigger immune responses.

While systemic pharmacologic inhibition of PP2A by inhibitors has been shown to increase sensitivity to ICB (42, 43), and KD of PPP2R2D (a B regulatory subunit of PP2A) in T cells enhances the cytotoxic function T cells in melanoma models (44), the effects of intrinsic PPP2R2A deficiency on ICB remain unexplored. The cGAS-STING-IFN pathway is important for ICB efficacy. Consistent with the increased cGAS-STING-IFN pathway in PPP2R2A deficient cells, we found that heterozygosity of *PPP2R2A* in tumors is associated with increased sensitivity to PD-L1 blockade. This activation influences immune cell recruitment and their activity, including NK and Tregs, even before PD-L1 antibody treatment. However, the cGAS-STING-IFN activation may extend beyond tumor cells; cytosolic DNA from tumor cells can be taken up by neighboring immune cells, thereby triggering cGAS-STING activation in immune cells (45). Consequently, the cGAS-STING and IFN signaling in immune cells may also enhance the efficacy of PD-L1 blockade in PPP2R2A-deficient tumors.

Supporting the role of type I IFNs in the antitumor activity of PD-L1 antibodies in tumors with PPP2R2A deficiency, we show here that the blockade of type I IFNs signaling via blocking IFNAR negated the increased sensitivity to PD-L1 antibodies observed in mice bearing *Ppp2r2a*$^{+/-}$ tumors. However, our study also highlights that while cytosolic DNA is essential for

cGAS-STING activation, type I IFN expression may not always be evident. For example, despite RS, cytosolic DNA accumulation, and cGAS-STING activation in LLC cells with PPP2R2A deficiency, type I IFN expression was not upregulated for reasons that remain unclear. This finding underscores the importance of assessing the integrity of the entire cGAS-STING-IFN axis rather than relying solely on cGAS-STING activation as a biomarker.

Although systemic pharmacological PP2A inhibition may not fully replicate the effects of PPP2R2A inactivation, preclinical models show significant synergy between PP2A inhibitors and PD-1 therapy (42, 43, 46). For example, LB-100, a direct PP2A inhibitor, enhances ICB sensitivity in mouse colon and melanoma models by activating mTORC1 signaling, which reduces the differentiation of naïve CD4 cells into Tregs. Additionally, PP2A inhibition also increases neoantigen expression by altering mRNA splicing (47) and promotes microsatellite instability through epigenetic silencing (48). Tumors with high genomic instability often exhibit elevated neoantigen expression. Our study suggests that *PPP2R2A* heterozygosity induces RS, DNA damage and genomic instability in tumor cells, which may explain the increased TMB observed in PPP2R2A-deficient NSCLC based on analyses of TCGA cohorts. Therefore, it is plausible that PPP2R2A deficiency also influences neoantigen expression and perhaps TMB, with multiple potential impacts on ICB outcomes.

It is important to note that NSCLC is a heterogeneous disease often driven by specific oncogenic mutations, which distinguish its subtypes. In clinical practice, analyzing multiple tumor mutations is recommended due to the therapeutic implications of drugs targeting EGFR, KRAS, ALK, ROS1, BRAF, NTRK1/2/3, MET, or RET (49). Tumors with these driver mutations exhibit distinct clinical characteristics compared to other tumors, and immunotherapy is typically not the first-line treatment (50). Therefore, it would be intriguing to investigate the impact of PPP2R2A deficiency in specific NSCLC subtypes, both with and without oncogene driver mutations. Further studies are needed to evaluate the outcomes of combining PD-L1 blockade with standard therapies, such as chemotherapy, radiation therapy or targeted therapies, in treating PPP2R2A-deficient NSCLC. Such investigations could provide valuable insights into optimizing therapeutic strategies for this subset of patients with lung cancer.

Type I IFNs respond to viral infection and regulate antitumor activity by modulating innate immunity, adaptive responses, and Tregs (51, 52). In PPP2R2A-deficient tumors, the most notable TME change is reduced Treg abundance and activity. Type I IFNs can affect Tregs directly or indirectly; our data show that intrinsic *Ifnar1* KO in Tregs reverses PD-L1 antibody-mediated antitumor activity in *Ppp2r2a*$^{+/-}$ tumors, indicating a Treg-intrinsic type I IFN pathway, though indirect effects cannot be excluded. While PPP2R2A deficiency has not been directly linked to immune antitumor activity, PP2A is essential for Treg function, and its loss disrupts metabolism and cytokine profiles, preventing suppression of effector responses (53). Pharmacologic PP2A inhibition (LB-100) combined with anti-PD-1 or CAR-T ICB induces durable antitumor responses in preclinical colon cancer, melanoma, and glioblastoma models (43, 54, 55). Moreover, inactivation of Ppp2r1a, the PP2A scaffolding subunit, promotes microsatellite instability, neoantigen production, and tumor immunogenicity in colorectal, breast, pancreatic cancers and ovarian clear cell carcinoma (48, 56). Thus, immune effects may differ among PP2A subunits, and the role of PPP2R2A deficiency in neoantigen production and ICB therapy warrants further study.

Although the roles of type I IFNs in regulating Tregs remain unclear and sometimes controversial, evidence links their antitumor activity to Treg modulation (52). IFN-α therapy has shown antitumor and immunomodulatory effects in cancers such as melanoma, partly by increasing tumor-infiltrating cells and reducing circulating Tregs (57). Tregs lacking IFNAR are less sensitive to type I IFNs (58). In human Tregs, IFN-α disrupts TCR signaling and suppresses cAMP induction, impairing Treg function (59). Recent studies also suggest that the functional stability and activity of $Foxp3^+$ Tregs are tightly regulated by cytokines (60). Other cytokines also shape Treg activity; for example, IL-6 downregulates Foxp3 and induces IL-17, whereas cytosolic dsDNA in tumor cells promotes CCL22-mediated Treg recruitment, despite reports that IFN-α inhibits CCL22(61). These opposing effects likely reflect Treg-extrinsic interferon activity(52) . Furthermore, PD-L1/PD-1 signaling has been shown to negatively regulate Tregs during infection (62, 63). Thus, PPP2R2A deficiency may suppress Treg activity through type I IFN– and PD-L1–mediated mechanisms.

In addition to Tregs, type I IFNs activate NK cells during antitumor responses, both directly and indirectly through other immune cells (51, 64). Investigating the effect of IFNAR-deficient NK cells on Ppp2r2a deficiency–induced ICB efficacy enhancement would be an interesting direction for future studies. Additionally, type I IFNs act in a complex manner. Type I IFN activity can either support or impair host defense, and that this dual effect is strongly influenced by when and how much IFN is produced, as well as the cellular context in which signaling occurs (65). In the future, identifying specific cytokines involved in promoting NK cell infiltration and suppressing Treg infiltration and activity will be a critical area of research.

PD-L1 is the first approved biomarker for anti-PD-1 therapy, but its predictive value is limited, as only ~45% of PD-L1-high NSCLC patients respond and some develop hyperprogression (66, 67). We found PPP2R2A deficiency increases PD-L1 via GSK3β and cGAS–STING, with the PPP2R2A/PD-L1 ratio correlating strongly with ICB outcomes, suggesting improved predictive accuracy. PPP2R2A deficiency also induces DNA damage and genomic instability; TCGA data confirm higher TMB in PPP2R2A-deleted NSCLC, though not clearly linked to poor prognosis. Since combining biomarkers may enhance prediction (68), PPP2R2A deficiency—through effects on PD-L1 and perhaps also TMB—represents a promising candidate. Supporting evidence includes PPP2R1A mutations associated with exceptional ICB response in ovarian cancer (69) and PP2A inhibition sensitizing tumors to PD-1/PD-L1, CTLA4, and CAR-T therapies (42).Thus, PPP2R2A deficiency warrants investigation as a predictive biomarker for ICB.

Conclusion

This study shows that cGAS–STING–IFN activation occurs in PPP2R2A-deficient cells without exogenous DNA damage. We reveal a link between PPP2R2A loss and PD-L1 expression and demonstrate its impact on Treg and NK cells in the TME. PPP2R2A deficiency both promotes and restrains antitumor immunity, and PD-L1–targeted ICB amplifies its positive effects, enhancing therapeutic efficacy. These results suggest PD-L1 ICB as a promising strategy for

PPP2R2A-deficient NSCLC and support PPP2R2A deficiency as a predictive biomarker for anti–PD-L1 therapy.

Materials and methods

Sex as a biological variable

Our study examined male and female animals, and similar findings are reported for both sexes.

Cell lines

H1299, HEK-293T, A549, CMT167 and LLC cells were cultured in DMEM medium (Hyclone); H1437 cells were cultured in 1640 medium (Hyclone) supplemented with 10% fetal bovine serum (FBS, Gibco) in a humidified atmosphere containing 5% CO_2 at 37°C. Cells that had been passaged ten times or less were used for experiments. CMT167 and LLC cells were gifts form Dr. Terrence Williams (City of Hope National Medical Center). All other cells were obtained from ATCC in 2016. Authentication was performed via STR profiling by the MCIC Genomics Core at Ohio State University in 2020. Mycoplasma contamination was ruled out in all cell lines using the LookOut Mycoplasma PCR Detection Kit (MP0035, Sigma) in 2020.

Generation of KO cells

Ppp2r2a KO were generated by using CRISPR/Cas9 technology. The CRISPR Design site http://crispor.tefor.net was used to identify guide RNA target sites flanking ENSMUSE00000267666 (exon 3) of the *Ppp2r2a* gene (NM_028032.3).

The following guide RNAs were used for mouse *Ppp2r2a* KO: – 5' GAACATCCTTAGTGAGTTGAGGG 3' for the 5' end of exon 3, and – 5' CCTCAGTAATAAGTTGACCTCTC 3' for the 3' end of exon 3. Oligonucleotides were phosphorylated and annealed and then cloned into *BsmBI* (ER0451, Fermentas) digested plasmid lentiCRISPR v2 (Plasmid #52961, Addgene). The lentivirus production and transduction were conducted according to the protocol from Addgene. Forward (5' TCCCAGGCTACAAGAGACCAC 3') and reverse (5' GCACAACACAGACATTTAAGGC 3') primers flanking the *Ppp2r2a* exon 3 and amplifying a product of 961 bp from the parental cells were used to characterize *Ppp2r2a* gene editing results in the single clones.

The following plasmids were used to generate the *STING* KO human and mouse cells: pLentiCRISPRv2-STING_gRNA3 (Plasmid #127640, Addgene) for human cells and pLentiCRISPRv2_mSTING_gRNA_1 (Plasmid # 196625, Addgene) for mouse cells.

The generation of *PPP2R2A* KO cells was as previously described (12).

Comet assay

Neutral comet assays were performed using the Comet Assay Kit (Trevigen, #4250-050-K) according to the manufacturer's protocol. Comet tail analysis was conducted utilizing TriTek CometScore software (version 2.0.0.38).

Plasmids

All shRNAs were obtained from Sigma Aldrich (**Supplementary Table 2**). pBabe GSK3β and pbabe GSK3β S9A were as previously described (12).

RNA extraction and real-time quantitative reverse transcription PCR

Total RNA was isolated using the RNeasy Mini Kit (74016, Qiagen) and subsequently treated with RNase-free DNase to eliminate genomic DNA contamination. Complementary DNA (cDNA) was synthesized from 1 μg of total RNA utilizing the Transcriptor First Strand cDNA Synthesis Kit (4897030001, Roche) with oligo(dT) primers. Real-time quantitative reverse transcription PCR (qRT-PCR) was performed as previously described. Primer sequences used for qRT-PCR are provided in the **Supplementary Table 3**.

Immunoblotting

Immunoblotting was conducted as previously described (10, 11). The primary antibodies used for Western blotting are listed in the **Supplementary Table 4**. Band intensities from Western blot images were quantified using ImageJ software (National Institutes of Health). Bands were selected using the Rectangle tool, and regions of interest (ROIs) were defined for each band. Pixel intensity was measured using the gel analysis function. Protein density values were normalized to the loading control β-Actin. The dilution for each antibody is shown in **Supplementary table** 4.

Immunofluorescence and cytosolic DNA staining

For cytosolic DNA staining, cells seeded on cover glasses were incubated with Pico488 (NC1878927, Lumiprobe) for 1 hour. After staining, the cover glasses were mounted and sealed using Antifade Mounting Medium with DAPI (H-1500-10, Vector Laboratories). Representative images were taken from a Zeiss LSM510 Meta confocal microscope.

Cytosolic DNA extraction and quantification

Cell fractionation was performed using NE-PER Nuclear and Cytoplasmic Extraction Reagents (78833, ThermoFisher). A SpectraMax Quant AccuClear Nano dsDNA Assay Kit (R8357, Molecular devices) and a BioTek Synergy H1 microplate reader were used to determine the concentration of cytosolic DNA.

Tumor models

Both male and female C57/BL6 mice (Strain code: 000664, The Jackson Laboratory), 6–8 weeks of age, were used for this study. The mice were bred at The Ohio State University (Columbus, OH). Xenografts were established by subcutaneous injections of CMT167 cells or LLC cells (1x 10^5 cells) with Matrigel (Cat: 356235, Corning) into the flank of the mice. Tumor diameters were measured with digital calipers, and volumes of the tumors were calculated using the following formula: Volume = $(\text{width})^2$ x length/2. Once tumor volume reached 50 mm^3, the mice were randomized into CMT167 *Ppp2r2a*$^{+/+}$ cells with control (Rat IgG2b *in vivo* Isotype Control, 100 μg/dose, Cat: ICH2243, Clone: 1-2, Ichorbio), *Ppp2r2a*$^{+/+}$ cells with α-PD-L1 (Anti-Mouse PD-L1 In Vivo Antibody, 100 μg/dose, Cat: ICH1086, Clone: 10F.9G2, Ichorbio), *Ppp2r2a*$^{+/-}$ with control and *Ppp2r2a*$^{+/-}$ with α-PD-L1. Treatments were given every two days

every two days for three doses. All mice were maintained under barrier conditions, and the experiments were conducted using protocols and conditions approved by the Institutional Animal Care and Use Committee (IACUC) of The Ohio State University.

Tissue digestion, cell isolation and flow cytometry

To isolate tumor, tissues were dissected and incubated for 20 minutes at 37℃ with collagenase D (1 mg/mL, 45-11088882001, Roche). Digested tissue was then filtered through a 40-μm nylon strainer (MSPP-15-1040, VWR). Blood cells were removed with RBC lysis buffer (420301, Biolegend). Cell suspension was washed by PBS. For flow cytometry staining, cells were washed twice in FACS buffer and FcR blocking was applied 10 minutes at 4℃. Live/dead staining was performed for 10 minutes at 4℃ with live/dead blue before staining with the surface antibody (described in **Supplementary Table 5**) mix for 30 minutes at 4℃ in FACS buffer. For intracellular staining, Foxp3/Transcription Factor Staining Buffer Set (00-5523-00, eBioscience) was used according to the manufacturer's protocol. Cells were then incubated with antibodies for 1-3 hours in permeabilization buffer. Samples were analyzed immediately on Cytek Aurora, and data analysis was performed using FlowJo (Tree Star) or OMIQ software (https://www.omiq.ai/).

Immune cell depletion assay

7 weeks C57/BL6 mice were implanted CMT167 *PPP2R2A*$^{+/-}$ cells as described. After nine days, mice were randomized to control (Rat IgG2b In Vivo Isotype Control, 100 μg/dose, Cat:ICH2243, Clone: 1-2, Ichorbio), α-PD-L1 alone (Anti-Mouse PD-L1 In Vivo Antibody, 100 μg/dose, Cat:ICH1086, Clone:10F.9G2, Ichorbio), α-PD-L1 + α-CD4 (Anti mouse CD4, 200 μg/dose, Cat: BP0003, Clone:GK1.5, BioXcell), α-PD-L1 + α-CD8 (Anti mouse CD8, 200 μg/dose, Cat: BP0004, Clone:53-6.7, BioXcell), α-PD-L1 + α-CD4/8 (Anti-CD4 + Anti-CD8 antibodies, 200 μg/dose for each antibody) and α-PD-L1 + α-NK (Anti-mouse NK1.1, 200 μg/dose, Cat: BP0036, Clone: PK136, BioXcell). Depletion antibodies were given on day 9 and day 11 after inoculation then twice weekly until endpoints. Control and PD-L1 antibodies were give on day 10, 12 and 14 after the inoculation of tumors.

IFNAR1 neutralization assay

CMT167 *Ppp2r2a*$^{+/+}$ and *Ppp2r2a*$^{+/-}$ cells were implanted in 7 week-old C57/BL6 mice as described. After nine days, mice were randomized to control alone (Rat IgG2b In Vivo Isotype Control, 100 μg/dose, Cat:ICH2243, Clone: 1-2, Ichorbio), α-PD-L1 alone (Anti-Mouse PD-L1 In Vivo Antibody, 100 μg/dose, Cat: ICH1086, Clone:10F.9G2, Ichorbio), control + α-IFNAR1 (Anti mouse IFNAR1, 200 μg/dose, Cat: BP0241, Clone: MAR1-5A3, BioXcell) and α-PD-L1 + α-IFNAR1. Antibodies were given on day 10, 12 and 14 after the inoculation of tumors.

Statistics

Statistical significance was assessed using GraphPad Prism 10.3 (GraphPad Software). Tumor growth curves were analyzed with repeated-measures two-way ANOVA. Survival analysis was conducted using the log-rank (Mantel-Cox) test. A two-tailed Student's *t*-test was used for comparisons between two groups. For multiple-group comparisons, one-way ANOVA followed

by Bonferroni post hoc analysis was applied when variance was not significantly different across groups. A P value of less than 0.05 was considered statistically significant.

Data availability

The bulk RNA-seq data have been deposited in the NCBI Gene Expression Omnibus (GEO) under accession number GSE311238. All values underlying the data presented in the graphs and as means are available in the Supporting Data Values file.

Study approval

All mouse studies were conducted under protocols approved by the IACUC of The Ohio State University (no. 2018A00000049).

Author contributions

JZ and ZL designed the study and JZ wrote the manuscript with critical input from ZL, ZQ, NS, AL and all the coauthors; ZQ, NS, AL, CP and XZ conducted experiments and acquired data; ZQ, NS, AL, DC, CB, CY, QW, XZ, ZL and JZ analyzed data. All authors reviewed and approved the manuscript.

Acknowledgement

This work is the result of NIH funding, in whole or in part, and is subject to the NIH Public Access Policy. Through acceptance of this federal funding, the NIH has been given a right to make the work publicly available in PubMed Central. The work described herein was supported by grants (R01 CA R01 CA240374, R01 CA249198, R21 CA226317), and the Lung Cancer Discovery Award, and DOD LCRP, W81XWH2010868 and Pelotonia Idea Award to J. Zhang from the National Cancer Institute and American Lung Association and U.S. Department of Defense and the Ohio State University James Comprehensive Cancer Intramural Research Program, respectively. Research reported in this publication was also supported by The Ohio State University Comprehensive Cancer Center (OSUCCC) and the National Institutes of Health (NIH) grants R01CA282501 and R01CA262069 (Z.L.). Additionally, this research was supported by the OSUCCC and the NIH (P30CA016058) and was made possible through resources, expertise, and support provided by the Pelotonia Institute for Immuno-Oncology (PIIO), which is funded by the Pelotonia community and the OSUCCC. We thank the PIIO and the Immune Monitoring and Discovery Platform for their contributions, especially related to high dimensional flow cytometry analysis. We also acknowledge the Flow cytometry shared resources (FCSR) and Genomic shared resources (GSR) at the OSUCCC for flow cytometry and sequencing services, respectively. The content is solely the responsibility of the authors and does not necessarily represent the official views of the National Institutes of Health.

References

1. Olivares-Hernandez A, Gonzalez Del Portillo E, Tamayo-Velasco A, Figuero-Perez L, Zhilina-Zhilina S, Fonseca-Sanchez E, et al. Immune checkpoint inhibitors in non-small cell lung cancer: from current perspectives to future treatments-a systematic review. *Ann Transl Med.* 2023;11(10):354.
2. Sangodkar J, Farrington CC, McClinch K, Galsky MD, Kastrinsky DB, and Narla G. All roads lead to PP2A: exploiting the therapeutic potential of this phosphatase. *FEBS J.* 2016;283(6):1004–24.
3. Ruediger R, Van Wart Hood JE, Mumby M, and Walter G. Constant expression and activity of protein phosphatase 2A in synchronized cells. *Mol Cell Biol.* 1991;11(8):4282–5.
4. Seshacharyulu P, Pandey P, Datta K, and Batra SK. Phosphatase: PP2A structural importance, regulation and its aberrant expression in cancer. *Cancer Lett.* 2013;335(1):9–18.
5. Kurimchak A, and Grana X. PP2A holoenzymes negatively and positively regulate cell cycle progression by dephosphorylating pocket proteins and multiple CDK substrates. *Gene.* 2012;499(1):1–7.
6. Ramos F, Villoria MT, Alonso-Rodriguez E, and Clemente-Blanco A. Role of protein phosphatases PP1, PP2A, PP4 and Cdc14 in the DNA damage response. *Cell Stress.* 2019;3(3):70–85.
7. Freeman AK, and Monteiro AN. Phosphatases in the cellular response to DNA damage. *Cell Commun Signal.* 2010;8:27.
8. Kalev P, Simicek M, Vazquez I, Munck S, Chen L, Soin T, et al. Loss of PPP2R2A inhibits homologous recombination DNA repair and predicts tumor sensitivity to PARP inhibition. *Cancer research.* 2012;72(24):6414–24.
9. Zhao Z, Kurimchak A, Nikonova AS, Feiser F, Wasserman JS, Fowle H, et al. PPP2R2A prostate cancer haploinsufficiency is associated with worse prognosis and a high vulnerability to B55alpha/PP2A reconstitution that triggers centrosome destabilization. *Oncogenesis.* 2019;8(12):72.
10. Qiu Z, Fa P, Liu T, Prasad CB, Ma S, Hong Z, et al. A Genome-Wide Pooled shRNA Screen Identifies PPP2R2A as a Predictive Biomarker for the Response to ATR and CHK1 Inhibitors. *Cancer Res.* 2020;80(16):3305–18.
11. Qiu Z, Sigh D, Liu Y, Prasad CB, Bean N, Yan C, et al. Low PPP2R2A expression promotes sensitivity to CHK1 inhibition in high-grade serous ovarian cancer. *Theranostics.* 2024;14(19):7450–69.
12. Singh D, Qiu Z, Jonathan SM, Fa P, Thomas H, Prasad CB, et al. PP2A B55alpha inhibits epithelial-mesenchymal transition via regulation of Slug expression in non-small cell lung cancer. *Cancer letters.* 2024;598:217110.
13. Yu WC, Chen HH, Qu YY, Xu CW, Yang C, and Liu Y. MicroRNA-221 promotes cisplatin resistance in osteosarcoma cells by targeting PPP2R2A. *Biosci Rep.* 2019;39(7).
14. O'Connor CM, Leonard D, Wiredja D, Avelar RA, Wang Z, Schlatzer D, et al. Inactivation of PP2A by a recurrent mutation drives resistance to MEK inhibitors. *Oncogene.* 2020;39(3):703–17.
15. Sun L, Wu J, Du F, Chen X, and Chen ZJ. Cyclic GMP-AMP synthase is a cytosolic DNA sensor that activates the type I interferon pathway. *Science.* 2013;339(6121):786–91.
16. Woo SR, Fuertes MB, Corrales L, Spranger S, Furdyna MJ, Leung MY, et al. STING-dependent cytosolic DNA sensing mediates innate immune recognition of immunogenic tumors. *Immunity.* 2014;41(5):830–42.

17. Chauvin SD, Stinson WA, Platt DJ, Poddar S, and Miner JJ. Regulation of cGAS and STING signaling during inflammation and infection. *The Journal of biological chemistry.* 2023;299(7):104866.
18. Ragu S, Matos-Rodrigues G, and Lopez BS. Replication Stress, DNA Damage, Inflammatory Cytokines and Innate Immune Response. *Genes (Basel).* 2020;11(4).
19. Chabanon RM, Rouanne M, Lord CJ, Soria JC, Pasero P, and Postel-Vinay S. Targeting the DNA damage response in immuno-oncology: developments and opportunities. *Nat Rev Cancer.* 2021;21(11):701–17.
20. Di Bona M, and Bakhoum SF. Micronuclei and Cancer. *Cancer Discov.* 2024;14(2):214–26.
21. Panicker N, Coutman M, Lawlor-O'Neill C, Kahl RGS, Roselli S, and Verrills NM. Ppp2r2a Knockout Mice Reveal That Protein Phosphatase 2A Regulatory Subunit, PP2A-B55alpha, Is an Essential Regulator of Neuronal and Epidermal Embryonic Development. *Front Cell Dev Biol.* 2020;8:358.
22. Mackenzie KJ, Carroll P, Martin CA, Murina O, Fluteau A, Simpson DJ, et al. cGAS surveillance of micronuclei links genome instability to innate immunity. *Nature.* 2017;548(7668):461–5.
23. Qiu Z, Fa P, Liu T, Prasad CB, Ma S, Hong Z, et al. A genome-wide pooled shRNA screen identifies PPP2R2A as a predictive biomarker for the response to ATR and CHK1 inhibitors. *Cancer research.* 2020.
24. Ablasser A, and Chen ZJ. cGAS in action: Expanding roles in immunity and inflammation. *Science.* 2019;363(6431).
25. Ablasser A, Goldeck M, Cavlar T, Deimling T, Witte G, Rohl I, et al. cGAS produces a 2'-5'-linked cyclic dinucleotide second messenger that activates STING. *Nature.* 2013;498(7454):380–4.
26. Li CW, Lim SO, Xia W, Lee HH, Chan LC, Kuo CW, et al. Glycosylation and stabilization of programmed death ligand-1 suppresses T-cell activity. *Nature communications.* 2016;7:12632.
27. Grabosch S, Bulatovic M, Zeng F, Ma T, Zhang L, Ross M, et al. Cisplatin-induced immune modulation in ovarian cancer mouse models with distinct inflammation profiles. *Oncogene.* 2019;38(13):2380–93.
28. Du SS, Chen GW, Yang P, Chen YX, Hu Y, Zhao QQ, et al. Radiation Therapy Promotes Hepatocellular Carcinoma Immune Cloaking via PD-L1 Upregulation Induced by cGAS-STING Activation. *Int J Radiat Oncol Biol Phys.* 2022;112(5):1243–55.
29. Tian Z, Zeng Y, Peng Y, Liu J, and Wu F. Cancer immunotherapy strategies that target the cGAS-STING pathway. *Front Immunol.* 2022;13:996663.
30. Hudson WH, Gensheimer J, Hashimoto M, Wieland A, Valanparambil RM, Li P, et al. Proliferating Transitory T Cells with an Effector-like Transcriptional Signature Emerge from PD-1(+) Stem-like CD8(+) T Cells during Chronic Infection. *Immunity.* 2019;51(6):1043–58 e4.
31. Gerlach C, Moseman EA, Loughhead SM, Alvarez D, Zwijnenburg AJ, Waanders L, et al. The Chemokine Receptor CX3CR1 Defines Three Antigen-Experienced CD8 T Cell Subsets with Distinct Roles in Immune Surveillance and Homeostasis. *Immunity.* 2016;45(6):1270–84.
32. Chen Y, Zander RA, Wu X, Schauder DM, Kasmani MY, Shen J, et al. BATF regulates progenitor to cytolytic effector CD8(+) T cell transition during chronic viral infection. *Nat Immunol.* 2021;22(8):996–1007.
33. Zander R, Schauder D, Xin G, Nguyen C, Wu X, Zajac A, et al. CD4(+) T Cell Help Is Required for the Formation of a Cytolytic CD8(+) T Cell Subset that Protects against Chronic Infection and Cancer. *Immunity.* 2019;51(6):1028–42 e4.
34. Kwon J, and Bakhoum SF. The Cytosolic DNA-Sensing cGAS-STING Pathway in Cancer. *Cancer Discov.* 2020;10(1):26–39.

35. Yu L, and Liu P. Cytosolic DNA sensing by cGAS: regulation, function, and human diseases. *Signal Transduct Target Ther.* 2021;6(1):170.
36. Xu B, Sun Z, Liu Z, Guo H, Liu Q, Jiang H, et al. Replication stress induces micronuclei comprising of aggregated DNA double-strand breaks. *PloS one.* 2011;6(4):e18618.
37. Dou Z, Ghosh K, Vizioli MG, Zhu J, Sen P, Wangensteen KJ, et al. Cytoplasmic chromatin triggers inflammation in senescence and cancer. *Nature.* 2017;550(7676):402–6.
38. Harding SM, Benci JL, Irianto J, Discher DE, Minn AJ, and Greenberg RA. Mitotic progression following DNA damage enables pattern recognition within micronuclei. *Nature.* 2017;548(7668):466–70.
39. Takaki T, Millar R, Hiley CT, and Boulton SJ. Micronuclei induced by radiation, replication stress, or chromosome segregation errors do not activate cGAS-STING. *Molecular cell.* 2024;84(11):2203–13 e5.
40. Sato Y, and Hayashi MT. Micronucleus is not a potent inducer of the cGAS/STING pathway. *Life Sci Alliance.* 2024;7(4).
41. Techer H, and Pasero P. The Replication Stress Response on a Narrow Path Between Genomic Instability and Inflammation. *Front Cell Dev Biol.* 2021;9:702584.
42. Clark MC, Lu RO, Ho WS, Dias MH, Bernards R, and Forman SJ. A combination of protein phosphatase 2A inhibition and checkpoint immunotherapy: a perfect storm. *Molecular oncology.* 2024;18(10):2333–7.
43. Ho WS, Wang H, Maggio D, Kovach JS, Zhang Q, Song Q, et al. Pharmacologic inhibition of protein phosphatase-2A achieves durable immune-mediated antitumor activity when combined with PD-1 blockade. *Nature communications.* 2018;9(1):2126.
44. Zhou P, Shaffer DR, Alvarez Arias DA, Nakazaki Y, Pos W, Torres AJ, et al. In vivo discovery of immunotherapy targets in the tumour microenvironment. *Nature.* 2014;506(7486):52–7.
45. Chen Q, Sun L, and Chen ZJ. Regulation and function of the cGAS-STING pathway of cytosolic DNA sensing. *Nat Immunol.* 2016;17(10):1142–9.
46. Ronk H, Rosenblum JS, Kung T, and Zhuang Z. Targeting PP2A for cancer therapeutic modulation. *Cancer Biol Med.* 2022;19(10):1428–39.
47. Dias MH, Liudkovska V, Montenegro Navarro J, Giebel L, Champagne J, Papagianni C, et al. The phosphatase inhibitor LB-100 creates neoantigens in colon cancer cells through perturbation of mRNA splicing. *EMBO Rep.* 2024;25(5):2220–38.
48. Yen YT, Chien M, Wu PY, Ho CC, Ho CT, Huang KC, et al. Protein phosphatase 2A inactivation induces microsatellite instability, neoantigen production and immune response. *Nature communications.* 2021;12(1):7297.
49. Chevallier M, Borgeaud M, Addeo A, and Friedlaender A. Oncogenic driver mutations in non-small cell lung cancer: Past, present and future. *World J Clin Oncol.* 2021;12(4):217–37.
50. Dantoing E, Piton N, Salaun M, Thiberville L, and Guisier F. Anti-PD1/PD-L1 Immunotherapy for Non-Small Cell Lung Cancer with Actionable Oncogenic Driver Mutations. *Int J Mol Sci.* 2021;22(12).
51. Muller L, Aigner P, and Stoiber D. Type I Interferons and Natural Killer Cell Regulation in Cancer. *Front Immunol.* 2017;8:304.
52. Piconese S, Pacella I, Timperi E, and Barnaba V. Divergent effects of type-I interferons on regulatory T cells. *Cytokine Growth Factor Rev.* 2015;26(2):133–41.

53. Apostolidis SA, Rodriguez-Rodriguez N, Suarez-Fueyo A, Dioufa N, Ozcan E, Crispin JC, et al. Phosphatase PP2A is requisite for the function of regulatory T cells. *Nat Immunol.* 2016;17(5):556–64.
54. Cui J, Wang H, Medina R, Zhang Q, Xu C, Indig IH, et al. Inhibition of PP2A with LB-100 Enhances Efficacy of CAR-T Cell Therapy Against Glioblastoma. *Cancers (Basel).* 2020;12(1).
55. Maggio D, Ho WS, Breese R, Walbridge S, Wang H, Cui J, et al. Inhibition of protein phosphatase-2A with LB-100 enhances antitumor immunity against glioblastoma. *J Neurooncol.* 2020;148(2):231–44.
56. Dai Y, Knisely A, Yano M, Dang M, Hinchcliff EM, Lee S, et al. PPP2R1A mutations portend improved survival after cancer immunotherapy. *Nature.* 2025;644(8076):537–46.
57. Di Trolio R, Simeone E, Di Lorenzo G, Buonerba C, and Ascierto PA. The use of interferon in melanoma patients: a systematic review. *Cytokine Growth Factor Rev.* 2015;26(2):203–12.
58. Pace L, Vitale S, Dettori B, Palombi C, La Sorsa V, Belardelli F, et al. APC activation by IFN-alpha decreases regulatory T cell and enhances Th cell functions. *J Immunol.* 2010;184(11):5969–79.
59. Bacher N, Raker V, Hofmann C, Graulich E, Schwenk M, Baumgrass R, et al. Interferon-alpha suppresses cAMP to disarm human regulatory T cells. *Cancer research.* 2013;73(18):5647–56.
60. Barbi J, Pardoll D, and Pan F. Treg functional stability and its responsiveness to the microenvironment. *Immunol Rev.* 2014;259(1):115–39.
61. Kim J, Pena JV, McQueen HP, Kong L, Michael D, Lomashvili EM, et al. Downstream STING pathways IRF3 and NF-kappaB differentially regulate CCL22 in response to cytosolic dsDNA. *Cancer Gene Ther.* 2024;31(1):28–42.
62. Perry JA, Shallberg L, Clark JT, Gullicksrud JA, DeLong JH, Douglas BB, et al. PD-L1-PD-1 interactions limit effector regulatory T cell populations at homeostasis and during infection. *Nat Immunol.* 2022;23(5):743–56.
63. Franceschini D, Paroli M, Francavilla V, Videtta M, Morrone S, Labbadia G, et al. PD-L1 negatively regulates CD4+CD25+Foxp3+ Tregs by limiting STAT-5 phosphorylation in patients chronically infected with HCV. *J Clin Invest.* 2009;119(3):551–64.
64. Swann JB, Hayakawa Y, Zerafa N, Sheehan KC, Scott B, Schreiber RD, et al. Type I IFN contributes to NK cell homeostasis, activation, and antitumor function. *J Immunol.* 2007;178(12):7540–9.
65. Fox LE, Locke MC, and Lenschow DJ. Context Is Key: Delineating the Unique Functions of IFNalpha and IFNbeta in Disease. *Front Immunol.* 2020;11:606874.
66. Shen P, Han L, Ba X, Qin K, and Tu S. Hyperprogressive Disease in Cancers Treated With Immune Checkpoint Inhibitors. *Front Pharmacol.* 2021;12:678409.
67. Wang DR, Wu XL, and Sun YL. Therapeutic targets and biomarkers of tumor immunotherapy: response versus non-response. *Signal Transduct Target Ther.* 2022;7(1):331.
68. Jiang Z, Zhou Y, and Huang J. A Combination of Biomarkers Predict Response to Immune Checkpoint Blockade Therapy in Non-Small Cell Lung Cancer. *Front Immunol.* 2021;12:813331.
69. Hinchcliff E, Patel A, Fellman B, Yuan Y, Chelvanambi M, Wargo J, et al. Loss-of-function mutations in PPP2R1A Correlate with Exceptional Survival in Ovarian Clear Cell Carcinomas Treated with Immune Checkpoint Inhibitors (099). *Gynecologic Oncology.* 2022;166:S66.

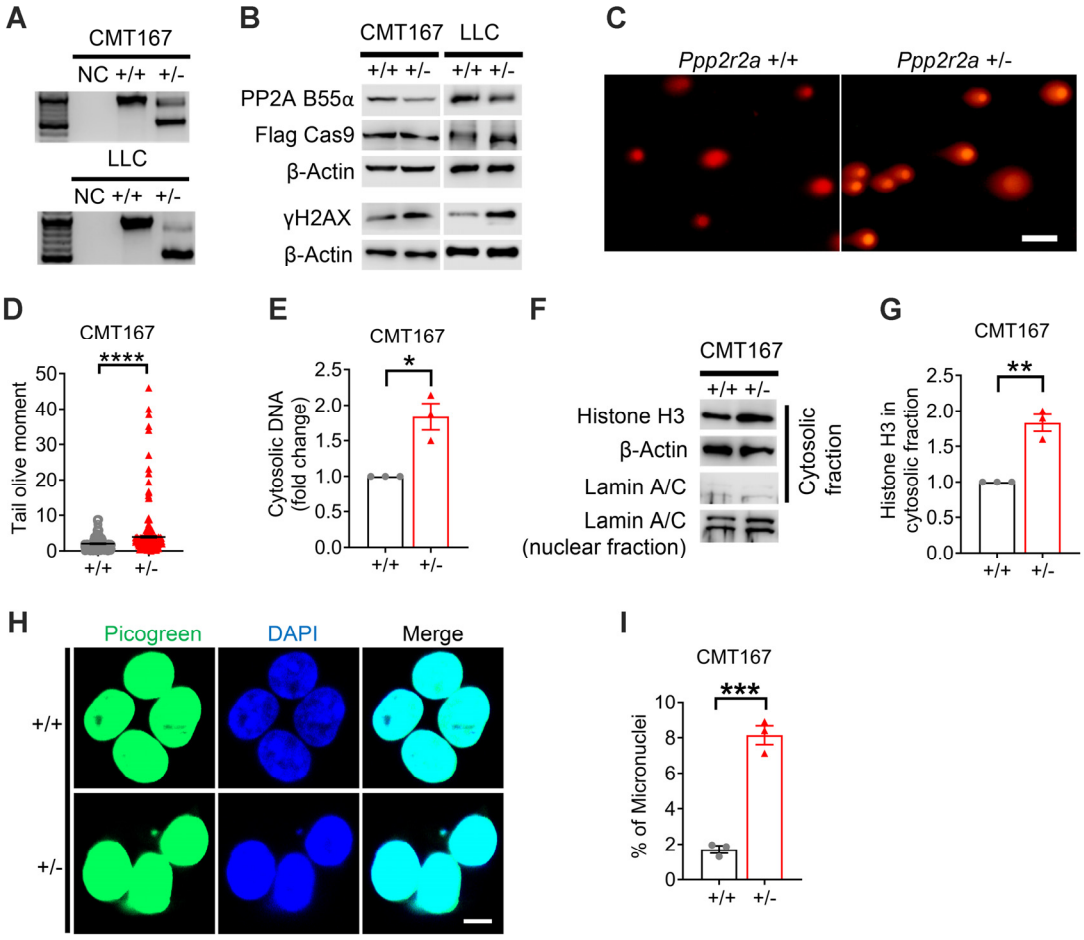

Figure 1. Monoallelic PPP2R2A KO leads to cytosolic DNA accumulation. (A–B) Genotyping and representative Western blot of *Ppp2r2a*$^{+/+}$ and *Ppp2r2a*$^{+/-}$ CMT167 and LLC cells. (**C–D**) Neutral comet assays showing DNA double-strand breaks. Data are represented as mean ± SEM from three biological repeats (n = 300) in **D**. (**E–I**) Quantification of cytosolic DNA, cytosolic Histone H3, and micronuclei in CMT167 cells. Data represent mean ± SEM (n = 3); *P < 0.05, **P < 0.01, ***P < 0.001, ****P < 0.0001 by Student's t-test. Scale bar, 200 μm in **C** and 30 μm in **H**.

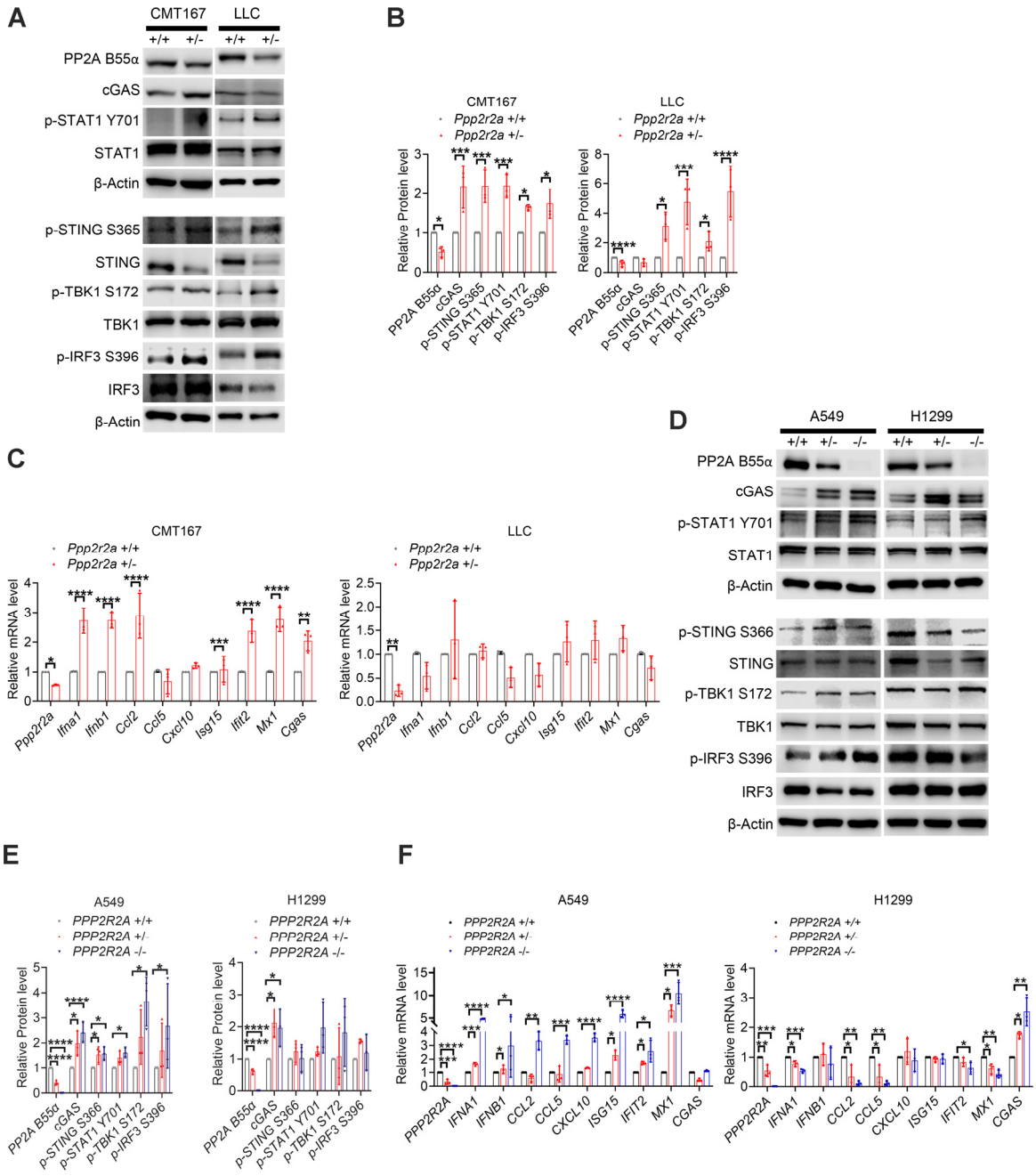

Figure 2. PPP2R2A KO activates type I IFN signaling. (**A**) Representative Western blot of cGAS–STING pathway proteins in CMT167 and LLC cells. (**B**) Quantification of protein levels from **A**. (**C**) qPCR of cGAS–STING and IFN-related genes in CMT167 and LLC cells. (**D**) Representative Western blot of cGAS–STING pathway proteins in A549 and H1299 cells. (**E**) Quantification of protein levels from **D**. (**F**) qPCR of cGAS–STING and IFN-related genes in

A549 and H1299 cells. Data represent mean ± SEM (n = 3); *P < 0.05, **P < 0.01, ***P < 0.001, ****P < 0.0001 by Student's t-test or one-way ANOVA with Bonferroni post hoc test.

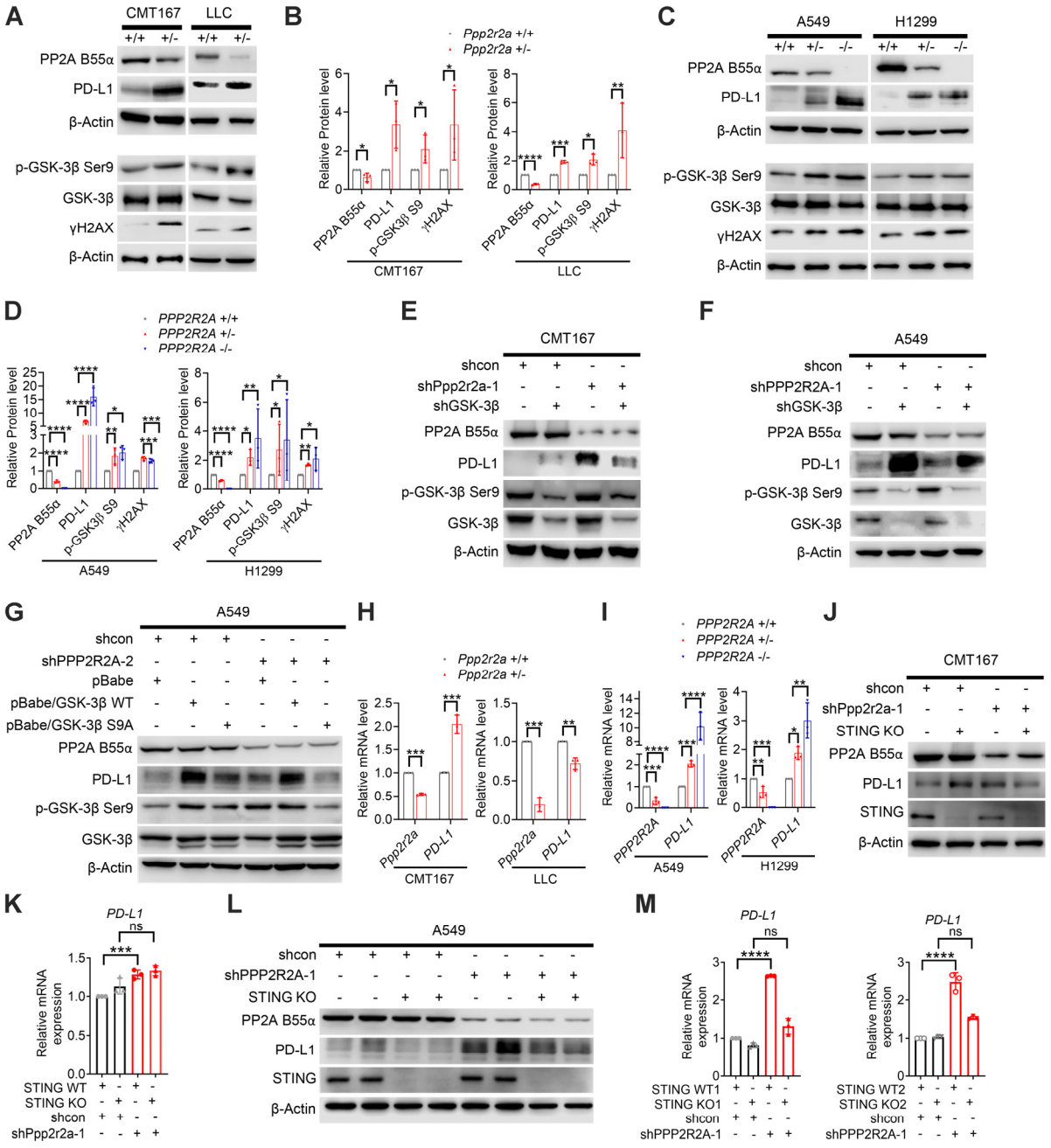

Figure 3. PPP2R2A deficiency increases PD-L1 expression. (**A–D**) Representative Western blot analysis showing increased PD-L1 protein levels in mouse (CMT167, LLC) and human (A549, H1299) cells after PPP2R2A KO, with quantification from biological replicates. (**E–G**) PD-L1 induction by PPP2R2A KD is dependent on GSK-3β phosphorylation. (**H–I**) qPCR of PD-L1 mRNA in human and mouse cells. (**J–M**) PD-L1 upregulation by PPP2R2A KD requires STING in CMT167 and A549 cells. ns, non-significant; **P* < 0.05, ***P* < 0.01, ****P* < 0.001, *****P*

< 0.0001. Data shown as mean ± SD (*n* = 3); Student *t*-test in **B** and **H** was used for the data analysis. Statistical analysis in **D**, **I**, **K** and **M** was conducted using one-way ANOVA followed by Bonferroni post hoc test for multiple comparisons.

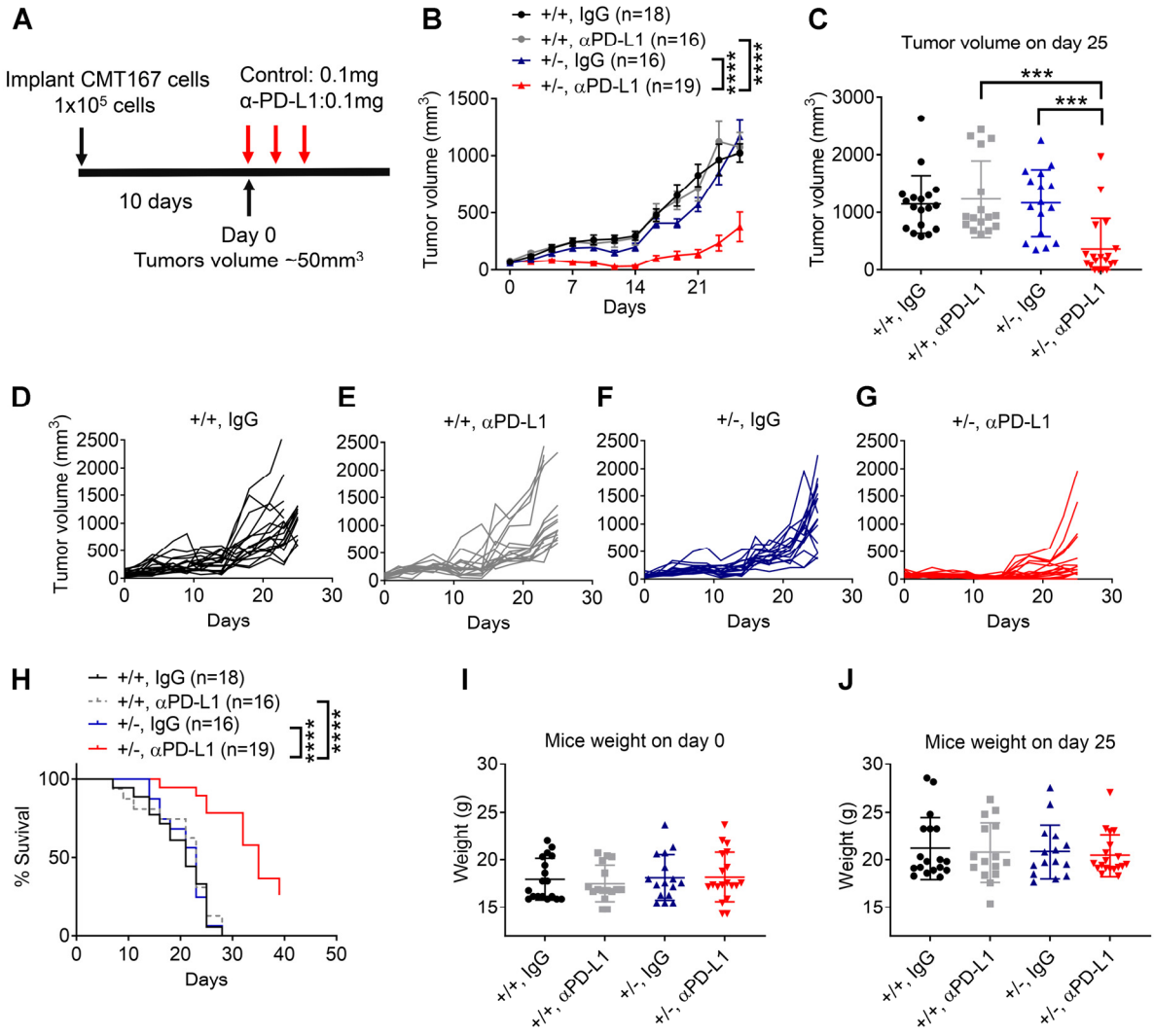

Figure 4. Ppp2r2a heterozygosity sensitizes CMT167 tumors to PD-L1 blockade *in vivo*. (**A**) Treatment schedule in mice bearing Ppp2r2a$^{+/+}$ or *Ppp2r2a*$^{+/-}$ tumors. (**B–G**) Tumor growth curves and individual tumor volumes with control or anti–PD-L1 antibody. (**H**) Kaplan–Meier survival analysis. ****, $P < 0.0001$, Kaplan–Meier analysis was used for overall survival. (**I–J**) Mouse body weights on day 0 and day 25. Data represent mean ± SEM; ***$P < 0.001$, ****$P < 0.0001$ by one- or two-way ANOVA with Bonferroni post hoc test.

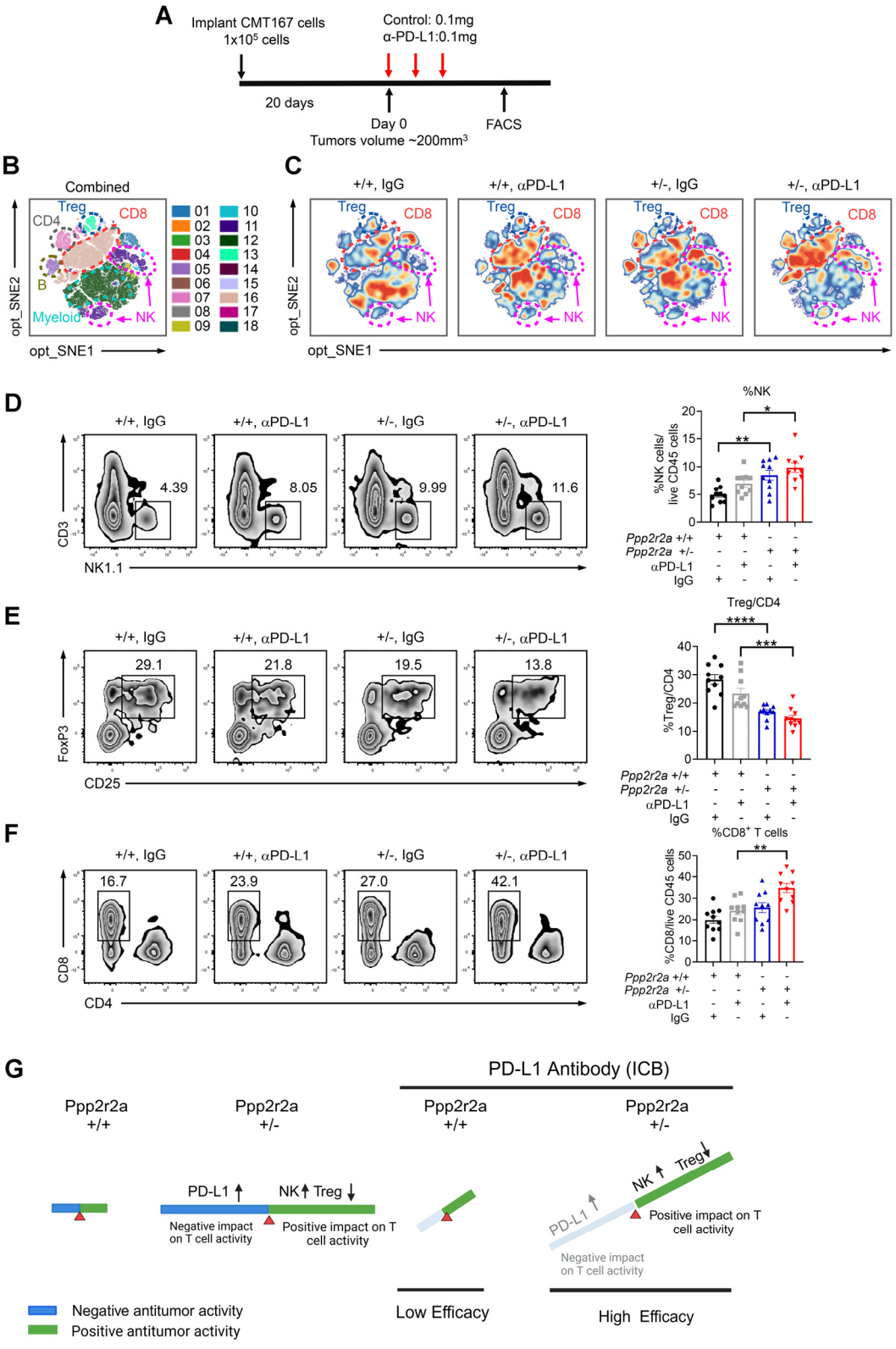
A
Implant CMT167 cells
1x10^5 cells
Control: 0.1mg
α-PD-L1:0.1mg
20 days
Day 0
Tumors volume ~200mm3
FACS
B
Combined
Treg
CD8
CD4
B
Myeloid
NK
opt_SNE2
opt_SNE1
01 02 03 04 05 06 07 08 09 10 11 12 13 14 15 16 17 18
C
+/+, IgG
+/+, αPD-L1
+/-, IgG
+/-, αPD-L1
D
CD3
NK1.1
4.39
8.05
9.99
11.6
%NK
%NK cells/ live CD45 cells
Ppp2r2a +/+
Ppp2r2a +/-
αPD-L1
IgG
E
FoxP3
CD25
29.1
21.8
19.5
13.8
Treg/CD4
%Treg/CD4
F
CD8
CD4
16.7
23.9
27.0
42.1
%CD8+ T cells
%CD8/live CD45 cells
G
PD-L1 Antibody (ICB)
Ppp2r2a +/+
Ppp2r2a +/-
PD-L1
NK
Treg
Negative impact on T cell activity
Positive impact on T cell activity
Low Efficacy
High Efficacy
Negative antitumor activity
Positive antitumor activity

1

Figure 5. **Ppp2r2a heterozygosity enhances anti–PD-L1 efficacy in CMT167 tumors by modulating immune cells**. (**A**) Treatment schedule for control antibody or anti–PD-L1 therapy followed by immune profiling. (**B–C**) Flow cytometry of $CD45^+$ tumor-infiltrating immune cells with opt-SNE and FlowSOM clustering. (**D–F**) Representative plots and quantification of NK, Treg, $CD4^+$, and $CD8^+$ T cell populations. Data represent mean ± SEM (n = 10); *P < 0.05, **P < 0.01, ***P < 0.001, ****P < 0.0001 by one-way ANOVA with Bonferroni post hoc test. (**G**) Schematic summary of TME reprogramming in PPP2R2A-deficient NSCLC under PD-L1 blockade.

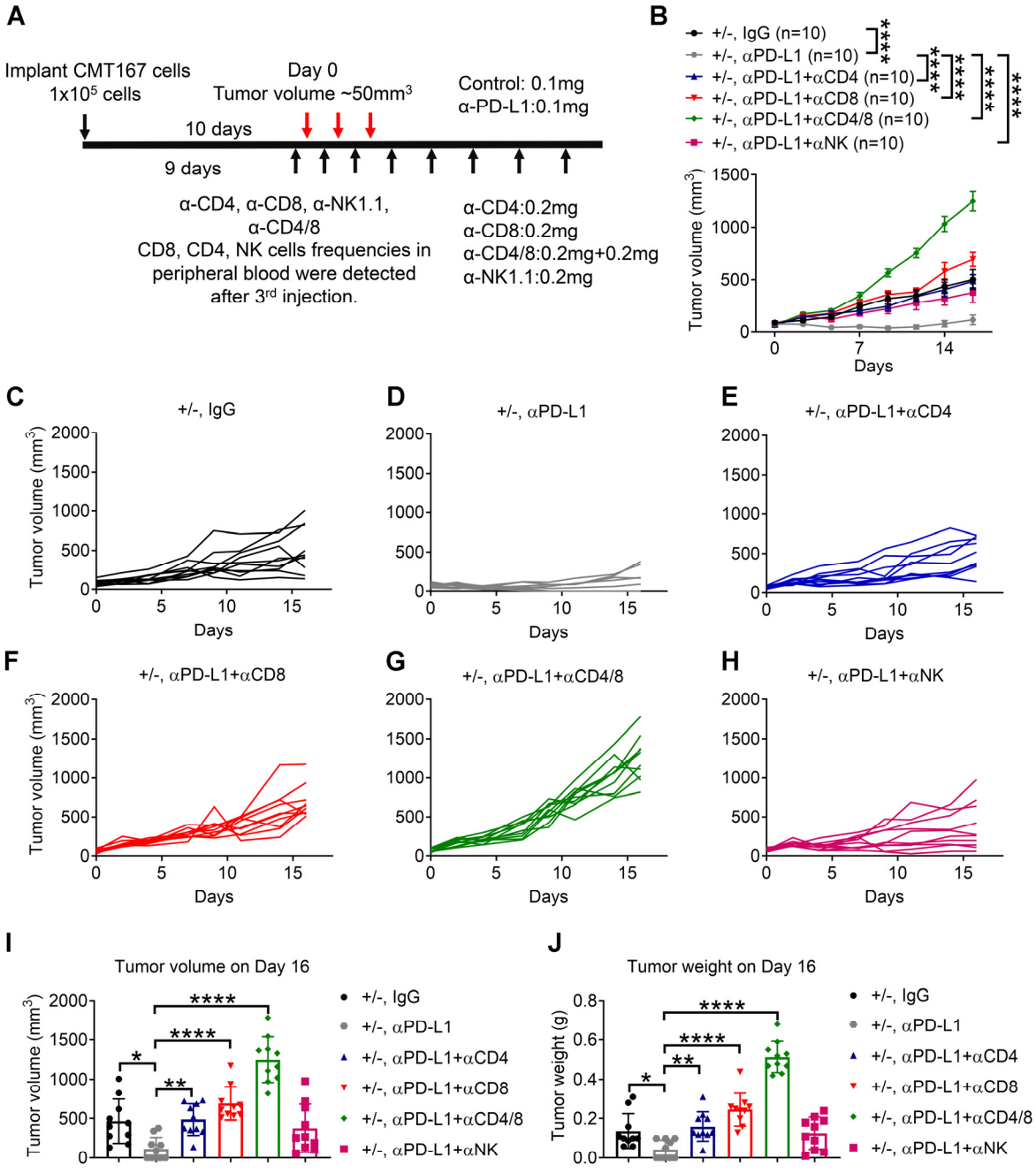

Figure 6. CD8⁺ T cells, CD4⁺ T cells, and NK cells are required for *Ppp2r2a* heterozygosity–mediated synergy with PD-L1 blockade. (**A**) Experimental design for immune cell depletion in CMT167 *Ppp2r2a*$^{+/-}$ tumors treated with control or PD-L1 antibodies. (**B–H**) Tumor growth curves showing loss of therapeutic efficacy upon depletion of CD4⁺, CD8⁺, or NK cells. (**I–J**) Quantification of tumor volumes and weights on day 16. Data represent mean

± SEM (n = 10); *P < 0.05, **P < 0.01, ****P < 0.0001 by one-way or two-way ANOVA with Bonferroni post hoc test.

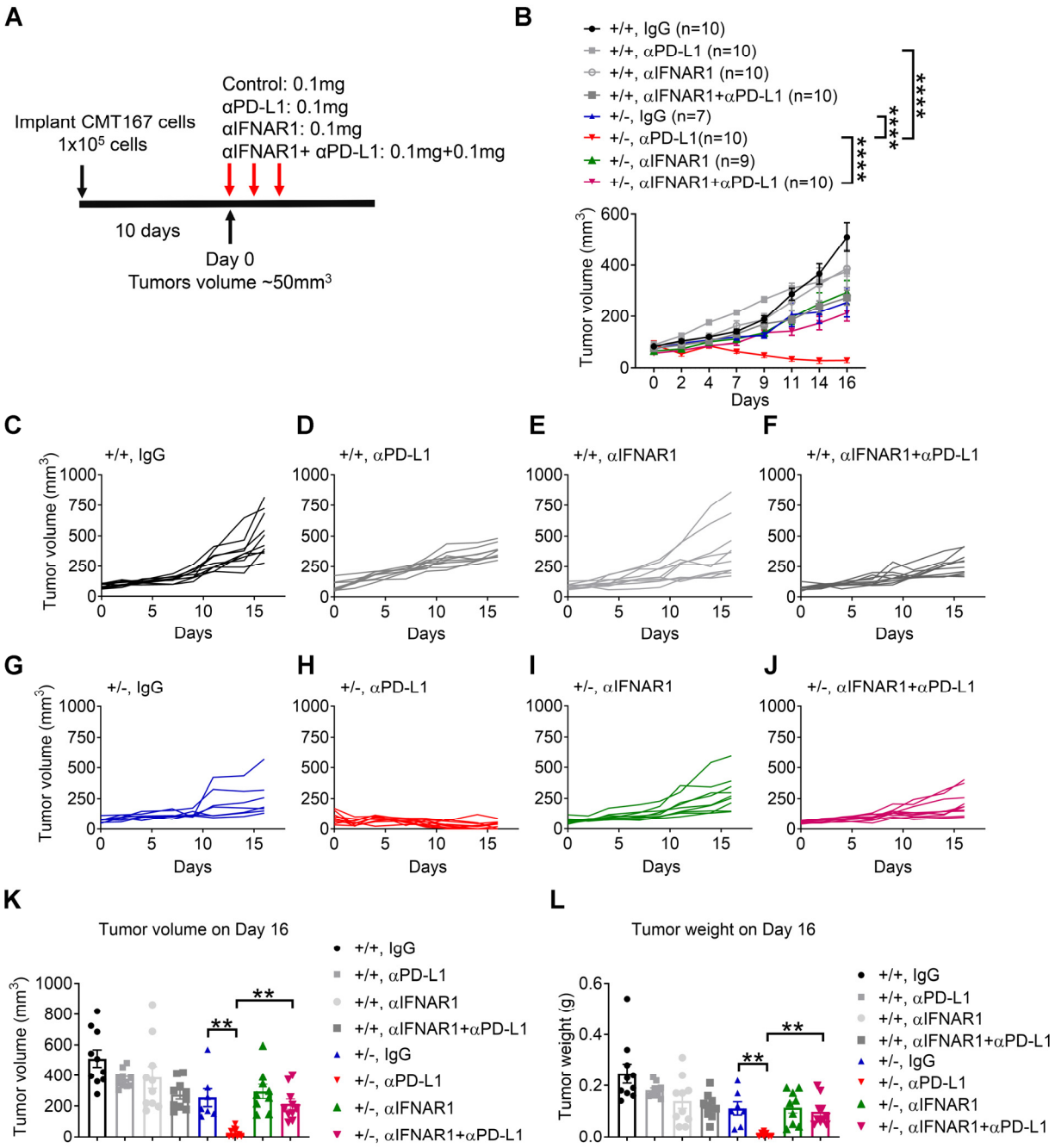

Figure 7. IFNAR1 neutralization abrogates PD-L1 blockade–induced regression in *Ppp2r2a*$^{+/-}$ tumors. (**A**) Treatment schedule in mice bearing *Ppp2r2a*$^{+/+}$ or *Ppp2r2a*$^{+/-}$ CMT167 tumors. (**B–J**) Tumor growth curves with control or anti–PD-L1 antibody ± IFNAR1 neutralization. (**K–L**) Quantification of tumor volumes and weights at endpoint. Data represent

mean ± SEM. (n = 10); **P < 0.01, ****P < 0.0001 by one-way or two-way ANOVA with Bonferroni post hoc test.

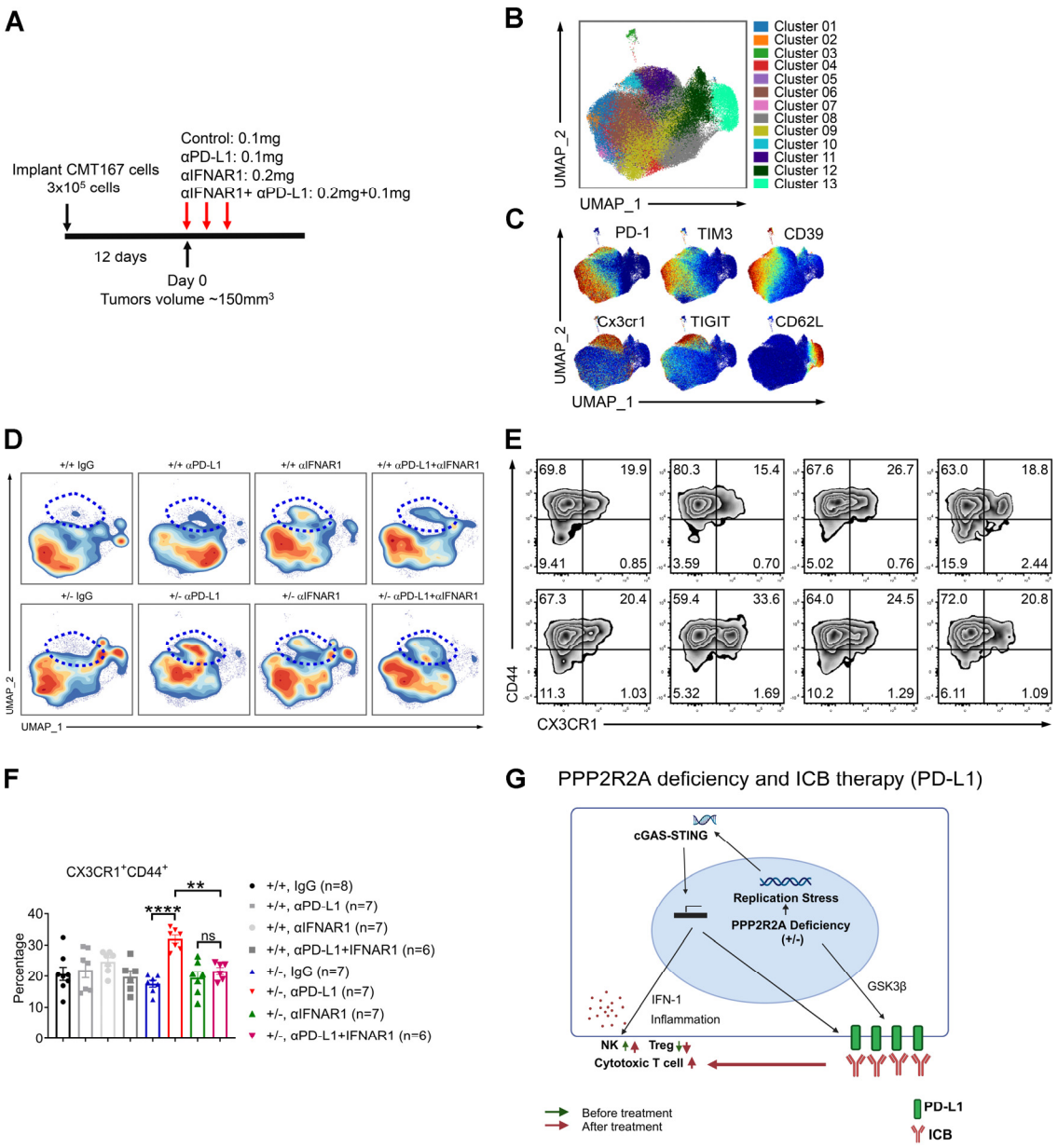

Figure 8. Type I IFN signaling drives cytotoxic CD8⁺ T cell expansion and the antitumor efficacy of PD-L1 blockade in Ppp2r2a+/- tumors. (**A**) Treatment schedule. (**B**) Visualization of CD8⁺ T cell flow cytometry data obtained from day 7 tumor samples. Tumor samples were collected from indicated groups and UMAP dimension reduction and FlowSOM clustering were applied to identify clusters with distinctive marker expression patterns. (**C**) Key marker expressions were overlaid onto UMAP space. (**D**) Contour plots were generated to display population dynamics across the groups. (**E**) Representative flow cytometry plot showing CX3CR1 and CD44 expression levels in CD8⁺ T cells. (**F**) Representative quantification of CD44⁺ CX3CR1⁺ CD8⁺ T cells. (**G**) Working model of PPP2R2A deficiency in ICB response.

Data represent mean ± SEM; ns, not significant; **$P < 0.01$, ****$P < 0.0001$ by Tukey's multiple comparison test.